

Complex Geodetic Monitoring of the Massive Sports Structures by Terrestrial Laser Scanning

Roman Shults ¹, Gulnur Seitkazina ^{2*}, Andriy Annenkov ³, Roman Demianenko ³,
Saule Soltabayeva ⁴, Zhenis Kozhayev ⁴, Gulizat Orazbekova ²

¹ Interdisciplinary Research Center for Aviation and Space Exploration, King Fahd University of Petroleum and Minerals, Dhahran 31261, Saudi Arabia.

² Department of Construction and Geodesy, Shakarim University, Semey 071412, Kazakhstan.

³ Department of Applied Geodesy, Kyiv National University of Construction and Architecture, 03037 Kyiv, Ukraine.

⁴ Department of Surveying and Geodesy, Satbayev University, 50013, Almaty, Kazakhstan.

Received 31 October 2024; Revised 11 February 2025; Accepted 17 February 2025; Published 01 March 2025

Abstract

The paper describes the rigorous approach to studying and analyzing the results of geodetic monitoring of massive sports structures. The monitoring results for two ski jumps in Almaty, Republic of Kazakhstan, are considered a case study. The suggested approach is based on the combined use of geodetic measurements and their comparative analysis with the structural analysis results of the structure using the finite element method. The structural analysis was carried out for various loads and their combinations, e.g., dead weight, snow load, wind load, etc. The article's aim is twofold. The first is to develop an appropriate algorithm and technology to accomplish geodetic monitoring, including the assignment of allowable monitoring accuracy. This goal was achieved by the results of structural analysis that helped to determine the allowable displacements and zones of maximum stress. These values defined the necessary observation accuracy and the places for the deformation targets' installation. Thus, the appropriate monitoring network around the complex of ski jumps was created. Geodetic monitoring was carried out using terrestrial laser scanning. Four observation epochs were conducted from autumn 2020 until summer 2022. The second aim is to analyze the monitoring results to determine the actual structure displacements and make conclusions concerning the allowance of these displacements for further structure exploitation. The monitoring results were studied using the structural analysis and B-spline displacement simulation. The results demonstrated no significant displacements of the ski jump ramps. The displacements for landing hills reached 60 mm, which is the allowable value.

Keywords: Geodetic Monitoring; Structural Mechanics; Load; Displacement; Allowable Monitoring Accuracy; Terrestrial Laser Scanning; Spline Function; Finite Element Method.

1. Introduction

The sports structures are part and parcel of the modern city and play an essential role in the sports and leisure industries. These structures have various geometries and huge sizes and may be constructed in multiple environmental conditions. Diverse stadiums, arenas, racetracks, tracks, etc., have become ordinary elements serving sports entertainment and championships. Among these structures, ski jumps are objects constructed in adverse conditions due to the necessity of building them in predominantly mountainous regions. Ski jumps are subjected to various loads, except for massive dead weight. There are loads of excessive snow and wind, including extreme wind gusts, icing, temperature

* Corresponding author: g.seitkazina@shakarim.kz

<http://dx.doi.org/10.28991/CEJ-2025-011-03-05>



© 2025 by the authors. Licensee C.E.J, Tehran, Iran. This article is an open access article distributed under the terms and conditions of the Creative Commons Attribution (CC-BY) license (<http://creativecommons.org/licenses/by/4.0/>).

variations, seismicity, and probable surrounding landslides. All in all, these conditions lead to deformations and displacements that rationalize the special attention to exploiting such structures. The right solution is to deploy and conduct permanent geodetic monitoring. Such a system should provide accurate and reliable monitoring results. Modern geodetic monitoring is an inseparable part of structural health monitoring (SHM) systems [1-3], which, in turn, are part of BIM [4-6]. Of course, SHM covers miscellaneous parameters, while geodetic monitoring ensures purely geometric values (displacements, rolls, bending, inclination, etc.) and their kinematic derivatives, e.g., displacement velocity. However, these geometric values are indispensable for understanding the structure's health and making use of it during the building life cycle. In what follows, we will use the term "displacement" as a general definition of structure movements.

The problem of geodetic monitoring of engineering structures, including sports structures, is not a new challenge for applied geodesy. For years, many scientists from different parts of the world have been developing and deploying geodetic monitoring systems and working out various monitoring methods. The state-of-the-art geodetic methods allow us to observe spatial displacements with necessary accuracy and frequency. Let us have a glimpse at contemporary geodetic methods and monitoring examples. Over the years, an enormous amount of research has been devoted to monitoring high-rise buildings, bridges, and dams using GNSS technologies [7-9], airport infrastructure and bridges by image-assisted robotic total stations [10-12] and their combination with accelerometers, vibrometers, and geotechnical sensors [13-15], historical buildings using inclinometers and other geotechnical sensors [16, 17], dams and different city infrastructure by space and ground-based InSAR technology [9, 18, 19], and stadiums by total station, leveling, and sensors [20, 21]. We may conclude that the most popular and widespread monitoring methods are GNSS, total stations, leveling, space and ground-based InSAR, and geotechnical sensors. We have intentionally left terrestrial laser scanning behind the scope of this review because this technology was used in the presented study and needs more in-depth consideration.

For the last decades, terrestrial laser scanning (TLS) has occupied a significant niche in geodetic monitoring [22]. The technology has been developed and tested for miscellaneous applications of engineering structure monitoring. It is worth noting that TLS was successfully applied for cooling tower surface deformations [23-25], wind turbine tower deformations [26], inclination determination of tall chimneys [27-29], dams and their infrastructure monitoring [30-32], tunnel monitoring [33-35], bridge monitoring [36, 37], retaining structure monitoring [38], spatial shells and similar structure monitoring, e.g., roofs, trusses, etc., [39, 40], oil and gas infrastructure monitoring [41], and monitoring of ordinary buildings in adverse exploitation conditions, e.g., mining regions [42]. This list is by no means exhaustive, but it gives us an excellent overview of TLS applications for geodetic monitoring. It is worth mentioning the successful application of TLS for monitoring massive structures, e.g., large steel structures [43] or buildings made of concrete [44]. This paper will present the new application of TLS for monitoring sports structures, namely ski jumps. To apply TLS for the given task, we need to understand the monitoring procedure, design, and result analysis. Let us consider the difficulties of these stages and possible ways of eliminating them.

Monitoring begins with an appropriate flowchart. Such a flowchart must include all monitoring stages and envisage different monitoring schemes. A number of studies have suggested various approaches to flowchart design [31, 33, 38, 43]. Few studies have suggested monitoring flowcharts. These flowcharts are not generalizable and correspond to specific monitoring objects [24, 30, 45]. The feature of TLS data is their complex interpretability. Essential questions regarding the possible methods of displacement calculation remain uncertain. We can calculate displacements by comparing point clouds, models, or specific targets. Each of these cases yielded different values as the data were preprocessed differently. The generalized flowchart must comprise all possible pathways of displacement calculation. Thus, the practical aim is to suggest a general monitoring flowchart that can be applied for various structure monitoring regardless of size, geometry, or application.

Despite decades of research on TLS applications, less attention has been paid to monitoring design, especially observation accuracy. Existing studies have focused on posterior accuracy estimation using measurement results [24, 25, 27, 29, 31] or equipment specification [33, 40] but failed to develop the models of accuracy assignment before measurements. Unfortunately, many investigations present the measured displacements as taken for granted without accuracy estimation, e.g., [30, 31, 34, 40]. Whereas for massive structures, monitoring accuracy must be known before measuring to ensure the correct monitoring scheme and evaluate the final results. Moreover, monitoring accuracy governs the requirements for geodetic networks and measuring equipment. Therefore, knowing the preliminary accuracy is essential for monitoring design. To date, scant attention has been paid to preliminary accuracy determination. For example, one may find very general requirements in EM 1110-2-1009 [46]. These requirements determine the accuracy of the whole class of structures regardless of their type and size. The sources for the suggested values in EM 1110-2-1009 [46] remain unknown. In our previous work [47], we proposed assigning the necessary accuracy based on the results of structure simulation. For sports structures that have complex geometry, the best simulation strategy is employing the finite element method (FEM). Yet, simple structural mechanics equations are also possible for small and simple structures. The analysis of simulation results allows us to determine the most significant possible displacements. There is another advantage of the FEM application. TLS data are presented in the form of a point cloud, which can easily

be embedded into the FEM simulation procedure [48-50]. In such a way, we may simplify the deformation analysis. Having the expected total displacement, we may assign monitoring accuracy as a portion of total displacement. That, in turn, will allow us to design the appropriate observation scheme and choose equipment based on this value. Therefore, the first research task is developing the accuracy models and conducting the necessary FEM simulation to obtain preliminary monitoring accuracy.

The most challenging stage is TLS data analysis. The high redundancy of TLS data makes displacement calculation uncertain and unobvious. These issues become especially appreciable during multitemporal TLS data processing. The simple cloud-to-cloud comparison becomes inefficient so long as data for different observation epochs may have different spatial resolutions and gaps due to unpredictable obstacles (people, assembling equipment, reconstruction works, etc.). For a correct understanding of the obtained displacements, it is necessary to have the analytical expressions that can be used further for prediction and deformation description. In geodesy, polynomial and Fourier series functions are very popular. However, these functions might not work well for TLS data when we need to describe the deformations of complex curves and surfaces, which we mostly have for sports structures. The convenient solution in this case is the application of spline functions. The amount of spline types astounds. Name a few: "natural" spline, Hermite spline, smoothed spline, B-spline, t-spline, non-uniform rational B-splines (NURBS), and so on. Many recent studies have investigated the capabilities of different spline functions for curves and surface modeling using TLS data. Remarkably, the most popular are B-splines for curves and surface modeling [51-53]. B-splines and NURBS are prevalent for deformation modeling [54, 55]. Despite the spline functions being extremely widespread for TLS data simulation [56-58], their application for deformation analysis is still underexplored. Yet, there are no comparative studies on the efficiency of different spline functions for deformation modeling. Previous studies have failed to showcase the capabilities of spline functions for multitemporal displacement analysis using TLS data, which is the sense of geospatial monitoring. Recent works on deformation analysis [51, 53, 54] have focused on displacement simulation for a single observation epoch. Such an analysis describes the most straightforward case when we have a design (ideal) model and a deformed model from observations [41, 45, 51]. The question about comparing the deformed structure for different observation epochs remains unanswered. Furthermore, no clear conclusion exists on which spline function is preferable for deformation analysis. The main issue is that all analyzed studies consider one particular type of spline function. There is no quantitative comparison between spline functions and the algorithms used in their simulations. Consequently, it is impossible to recommend the required function for displacement simulation. So, the second scientific goal was to investigate different spline functions for deformation simulation and analysis and provide the necessary recommendations.

In general, this study was undertaken to determine the capabilities of TLS for monitoring sports structures. The practical testing of the suggested models and analysis approaches was accomplished using the "Sunkar" ski jump monitoring results. An FEM simulation of the ski jump structure was carried out to achieve the first aim. The simulation results were used to assign monitoring accuracy and check spline simulation results. The remainder of this paper is organized as follows. Section two reviews the monitoring object, flowchart, FEM simulation, and basic ideas of spline functions. Section three presents the new method and algorithms for accuracy assignment. Section four provides the results of geodetic monitoring, including the geodetic network and obtained displacements. The second part of this section investigates various spline functions and discusses the deformation analysis results.

2. Material and Methods

2.1. Monitoring Object – Sport Complex "Sunkar"

The "Sunkar" International Ski Jumping Complex monitoring project was selected to evaluate the efficiency of the suggested methods and algorithms. The sports complex is located in Almaty, the former capital of the Republic of Kazakhstan. The city is surrounded by mountainous hills that create favorable conditions for ski jump construction. On the other hand, steep and unstable hills are the source of landslide activity, severely threatening construction stability. Yearly, depending on the season, the sports complex undergoes different loads invoked by snowfalls, icing, and wind gusts. Moreover, the Almaty region is well-known as an area of high seismicity. This region has been subjected to permanent earthquakes (the last one occurred in Jan 2024), some of which have disastrous effects. These earthquakes lead to land movements, including landslides. This circumstance generates additional issues for the structure's exploitation during its life cycle. The complex has been built at a height of 900 m above sea level. There are five ski jumps that have different lengths and purposes. The longest ski jumps are K125 and K95, with lengths of 125 m and 95 m, respectively (Figure 1). These ski jumps have been selected to implement our ideas and further monitoring.

The construction scheme of both ski jumps is complex. The supportive structure is compounded from steel trusses. A concrete runway overlays this structure. A concrete-covered hill below is used for the landing. From a geometrical point of view, the ski jump ramp has sophisticated geometry, which in the first iteration can be represented as a parabola. To conclude, the complex is affected by various environmental loads that specify the necessity of geodetic monitoring. The successful accomplishment of the monitoring depends on achieving the required accuracy and correct analysis of the results.



Figure 1. Top (left) and side (right) views of the "Sunkar" ski jump complex

2.2. Monitoring Flowchart

In the introduction, we noted that TLS guarantees excellent monitoring capabilities, so we focused on this technology. The authors suggested and developed their monitoring flowchart based on analysis of various studies and their own experience [6, 59]. This flowchart takes into account that TLS is the primary measuring equipment selected for this study, and the measurement output is a point cloud. The suggested flowchart contains four primary stages: project design, fieldwork, data processing, and data analysis (Figure 2).

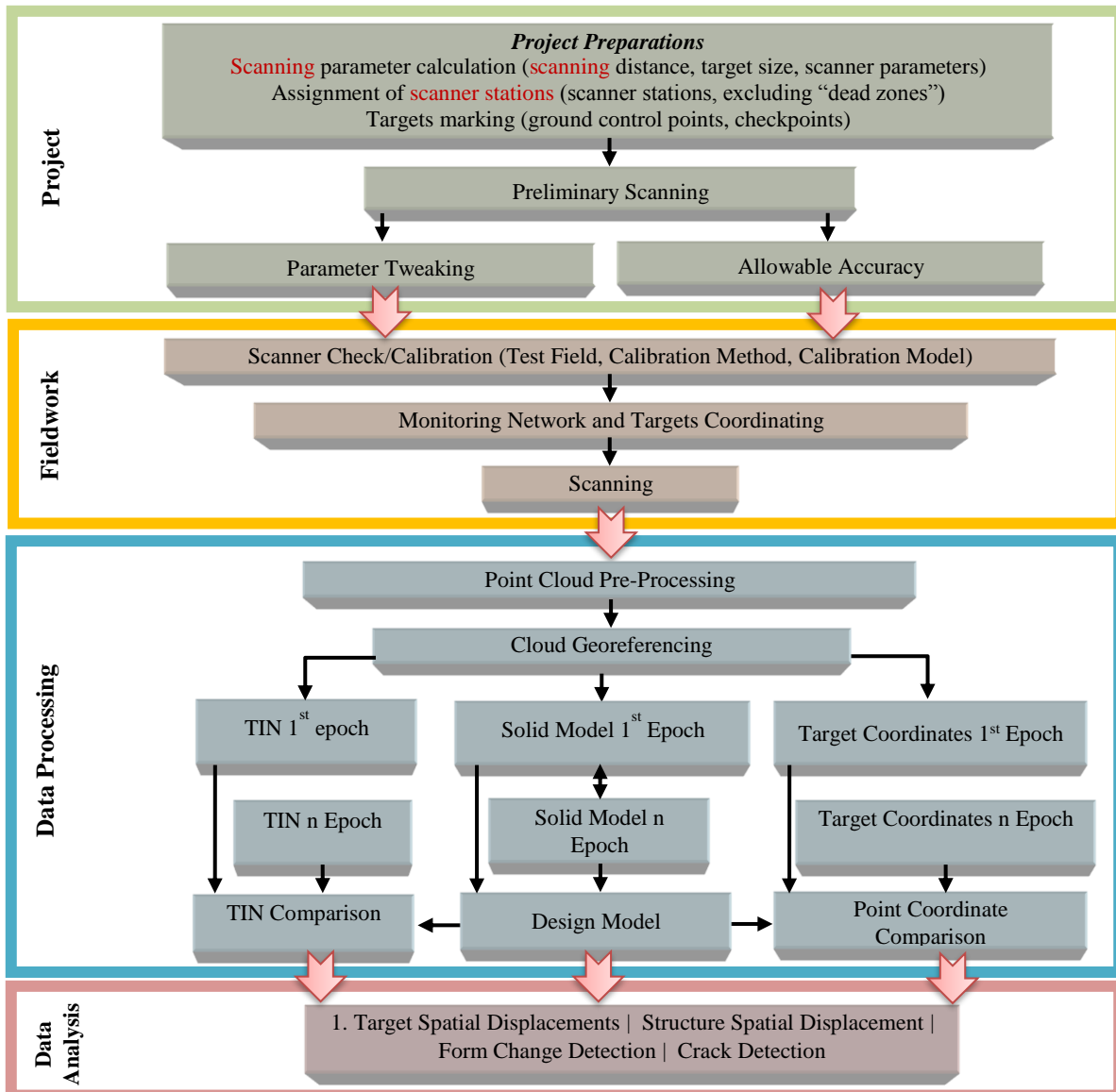


Figure 2. TLS monitoring flowchart

The design stage contains the following steps: parameter calculation, assignment of points, target marking, and the first sticking point–accuracy calculation. Namely, at this step, the surveyor must determine the accuracy of the measurements to ensure reliable monitoring results. Fieldwork includes the necessary measurement procedures to obtain point clouds for each observation epoch. The collected point clouds must be pre-processed and finally compared with each other, as well as the design model or any other model that can be considered as a reference. The outcomes of these comparisons are displacements for targets, specific points, curves, and surfaces. Here, we have the second bottleneck because, for the comparison, we require analytical functions describing the point displacements for each observation epoch. Therefore, we approach the final stage, where the flowchart feeds the displacements into the data analysis stage and delivers mathematical models describing the displacement changes in time. To find the solution to these two issues, we suggest applying FEM for accuracy calculation and spline functions for point displacements. Let us consider the features of these methods and briefly outline the math background behind these methods.

2.3. Finite Element Analysis

The algorithm of FEM is well-developed and computerized. There is no point in delving into the FEM principles and equations because anyone may find them in miscellaneous works. The theory of the FEM is described in a bunch of textbooks, scientific reports, and papers, e.g., [60-62]. Theoretically, the ski jumps’ ramps present the case of frames and trusses simulated by FEM [63]. Thus, without wasting time, let us get down to the FEM simulation analysis and present the most important results. As mentioned, the monitoring objects are two ski jumps, 95 m and 125 m long. Both ski jumps were partitioned into finite elements (beams) for the simulation. The dimensions of ski jump K125 are given in Figure 3.

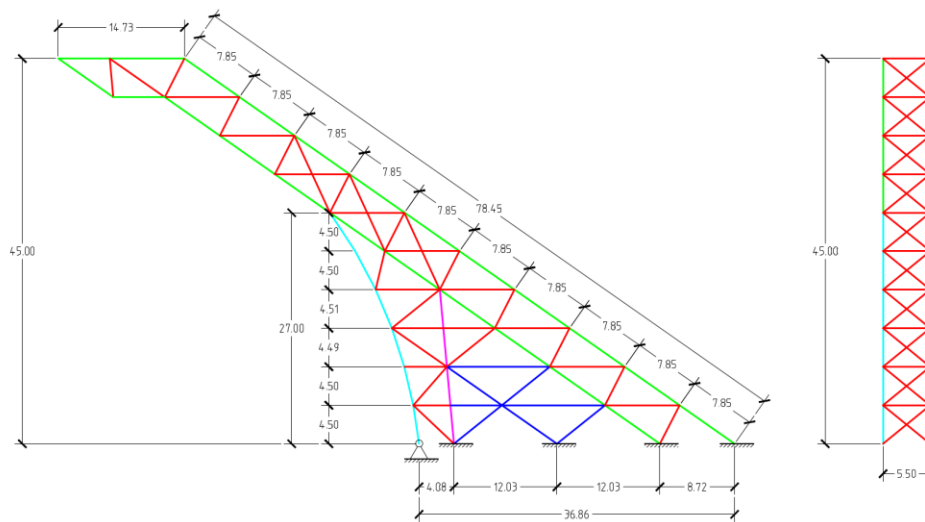


Figure 3. Primary dimensions (m) of the ski jump K125

The height of K95 is 18 m, while K125 is almost three times higher. The geometry of the ski jump K95 is the same, with a smaller number of elements. The results of dividing the ski jumps K95 and K125 into finite elements are presented in Figure 4.

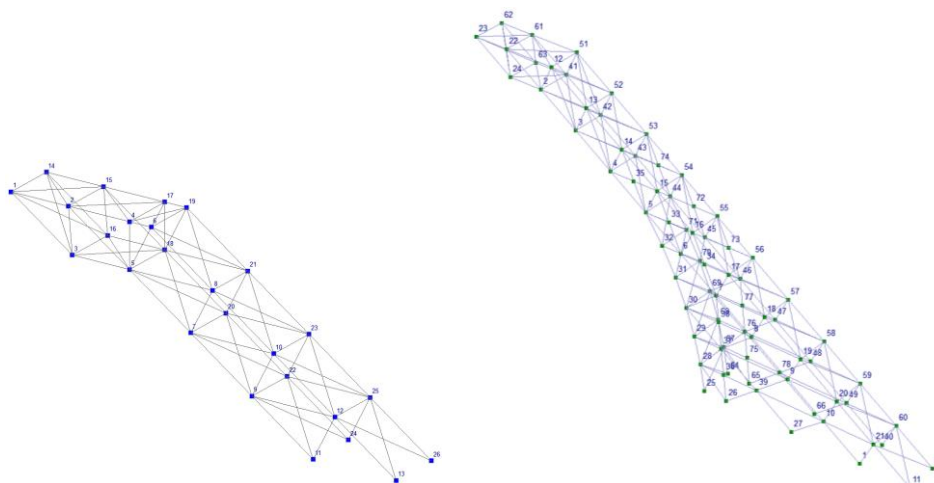


Figure 4. 3D scheme of the ski jumps K95 and K125 with node numbers

For the simulation, we must compile and exert the various loads on the structures. In total, K95 consists of 26 nodes and 81 beam elements. There are two types of element cross-sections with different stiffness. For K125, we have 77 nodes and 235 beam elements, with three types of cross-sections. The structures are subjected to the following loads: dead weight, snow weight, and wind load. The dead weight of the metal frame, plus the weight of the fence, is considered constant. Snow and wind loads are temporal. We took the worst case when the standard snow fell during the downtime between competitions (the snow was not cleared for a long time). For the given climate zone, 70 kg/m² of snow is applied to the upper inclined plane. The load is distributed evenly along the upper purlins. For wind load, we took the standard load from the windward side of 38 kg/m² and for the leeward side 22 kg/m². We assumed the entire wind load is conveyed to the truss belts, pylon posts, and transverse ties. Except for the considered loads, we analyzed specific cases of probable landslide effects. Let us suppose that points 1, 11, 40, and 50 for K125 (13 and 26 for K95) are subjected to vertical displacements due to land movements (Figure 5). The uniform and non-uniform displacement cases were considered.

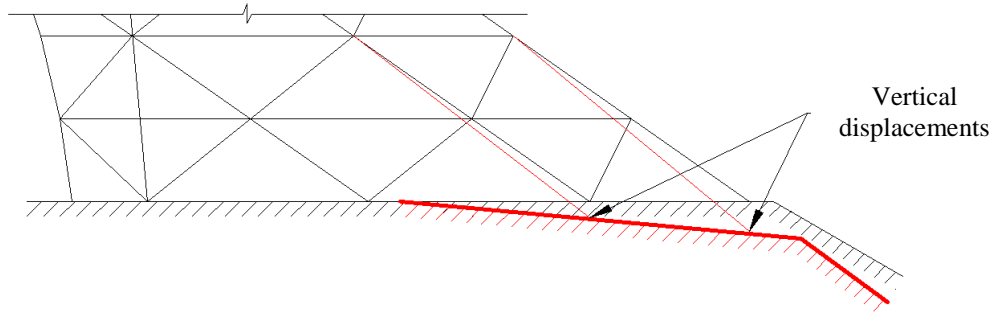


Figure 5. Diagram of displacements due to landslide

The simulation was accomplished for six different load cases. Consequently, the following cases were simulated: 1 – dead weight, 2 – snow load; 3 – wind load; 4 – dead weight, snow and wind loads; 5 – dead weight plus sediment in one point (100 mm); 6 – dead weight plus non-uniform displacements in two points (50 mm and 100 mm). Due to limited space, we cannot represent the whole set of the simulation results. For the problem of accuracy assignment, the primary role plays the value and distribution of maximum displacements. The extreme values of the displacements for K95 are summarized in Table 1.

Table 1. Extreme values of displacements for K95

Displacement	Maximum			Minimum		
	Value	Node	Load case	Value	Node	Load case
X, mm	136.8	6	6	-23.2	14	4
Y, mm	0.3	22	2	-181.7	1	5
Z, mm	248.0	14	6	-100.0	13	5
U _x , deg	0.684	14	5	-0.084	9	5
U _y , deg	0.703	12	6	-0.095	22	4
U _z , deg	0.353	12	5	-0.119	21	5

Figures 6 to 8 illustrate the displacements for case 6 along the coordinate axis, measured in millimetres.

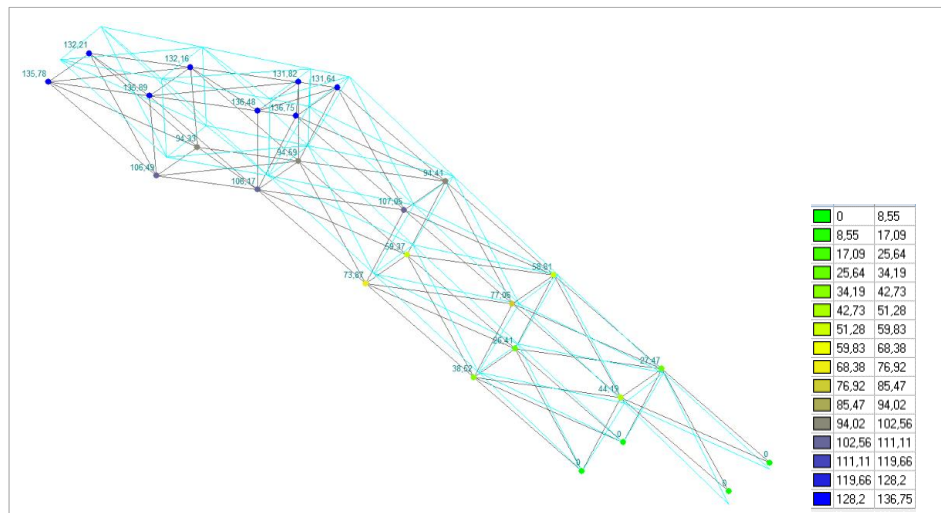


Figure 6. Diagram of displacements (mm): load case 6, axis X, K95

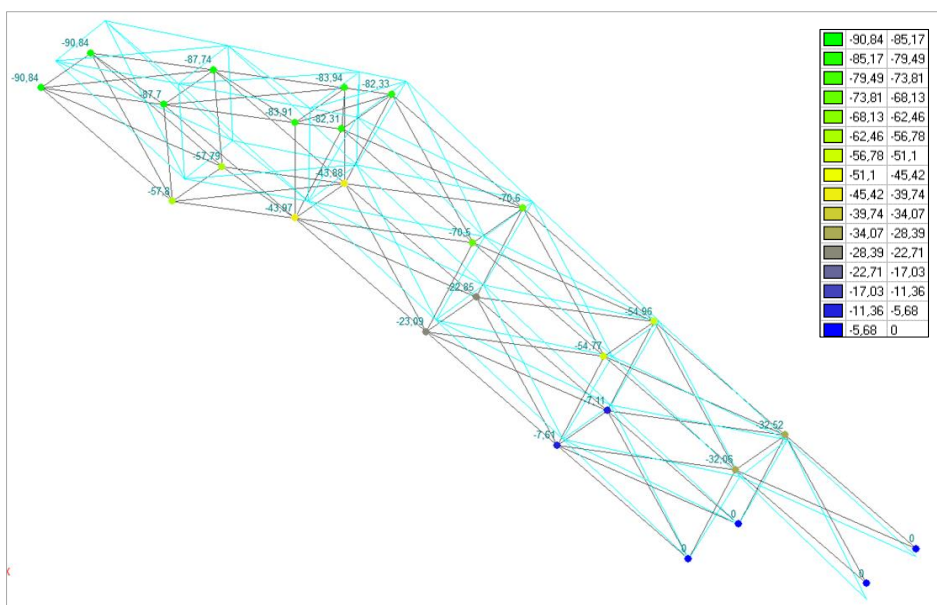


Figure 7. Diagram of displacements (mm): load case 6, axis Y, K95

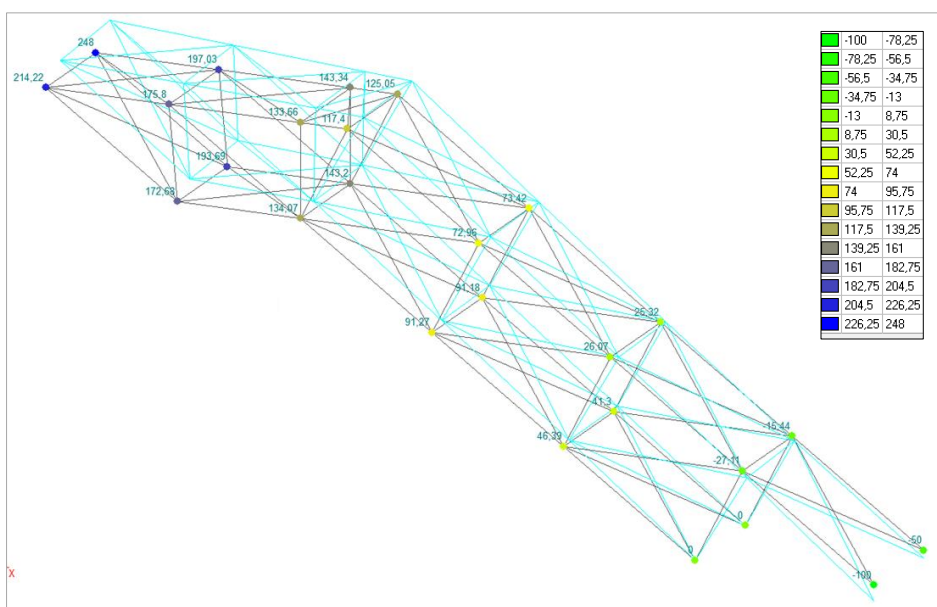


Figure 8. Diagram of displacements (mm): load case 6, axis Z, K95

The simulation results for K125 are also summarized in Table 2. A sample of displacement diagrams for K125 is provided below in Figures 9 to 11. The displacements are given in millimeters.

Table 2. Extreme values of displacements for K125

Displacement	Maximum			Minimum		
	Value	Node	Load case	Value	Node	Load case
X, mm	98.0	61	5	-28.5	62	1
Y, mm	1.6	47	2	-292.7	12	4
Z, mm	109.8	62	4	-100.0	11	4
U _x , deg	2.808	35	4	-0.443	47	3
U _y , deg	0.349	21	5	-0.094	24	1
U _z , deg	0.414	47	3	-1.879	72	4

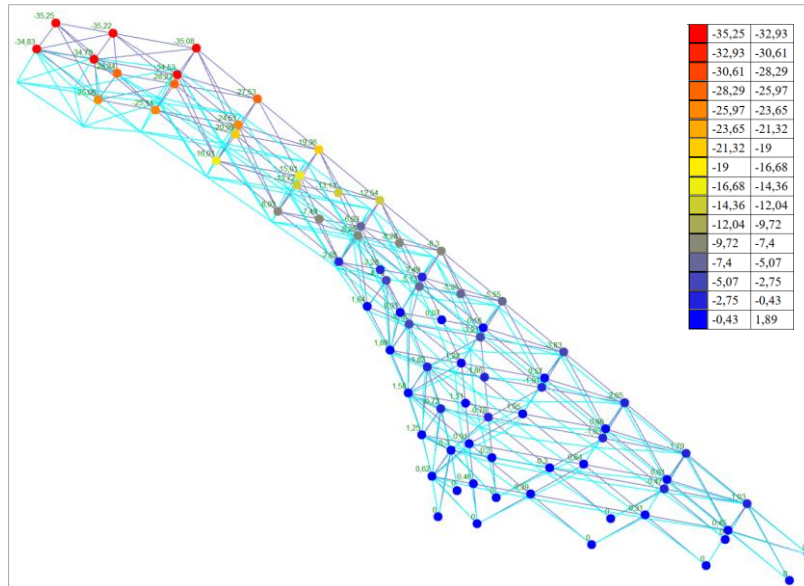


Figure 9. Diagram of displacements (mm): load case 4, axis X, K125

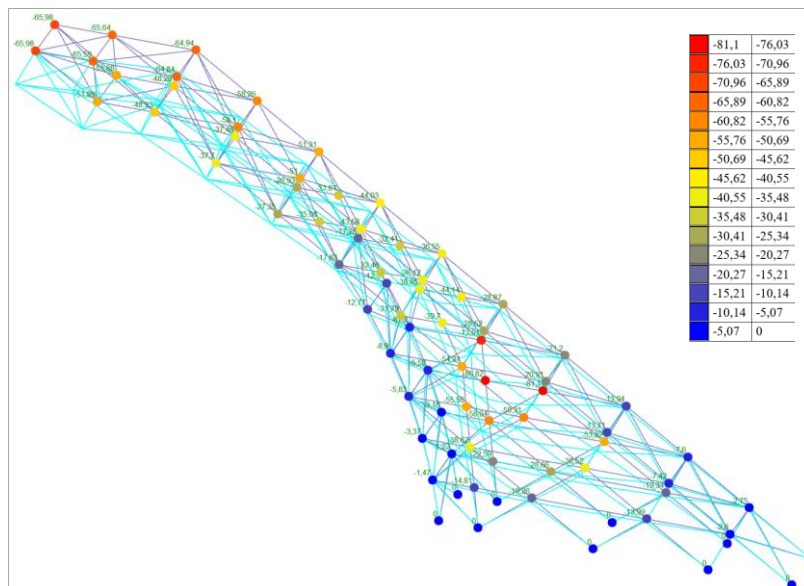


Figure 10. Diagram of displacements (mm): load case 4, axis Y, K125

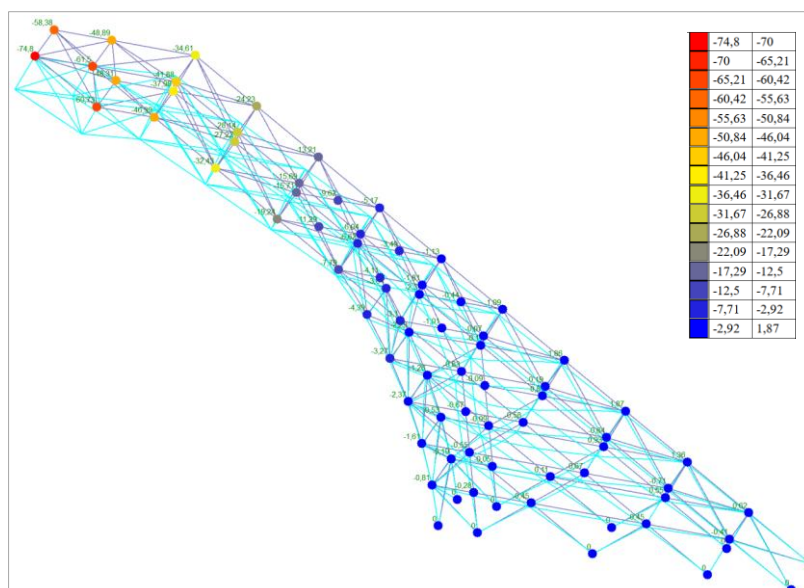


Figure 11. Diagram of displacements (mm): load case 4, axis Z, K125

The general conclusion from the simulation results confirms the high durability and stability of the ski jumps. However, the combination of extreme loads may lead to undesirable displacements. These displacements, in turn, may invoke non-reversible deformations, creating threats for further structure exploitation. Thus, geodetic monitoring is an indispensable measure required for safe structure operation. The accomplished simulations allowed us to obtain complete information about ski jump deformations under various loads. This information will be used for accuracy assignment and analysis of measured deformations during geodetic monitoring.

2.4. Spline Functions for Displacement Analysis

If the project envisages target marking, then it is possible to compare the coordinates of these targets to determine displacements. In all other cases, scanning results must be modeled before further comparison. Each monitoring epoch provides a unique point cloud. The measured points are distributed differently in this point cloud according to the scanning grid. Since we deal with different point clouds for each observation epoch, an interpolation function must be used to describe the spatial form of a surface/curve. We can compare the surface/curve for different monitoring epochs by having such a function. Thus, it is required to have the interpolation function that will pass through the measured points and represent the surface/curve form well. The best solution for this task is the application of spline functions. The problem behind the spline function application is its correct mathematical form choice. For years, mathematicians and engineers have worked out a lot of various spline versions. To choose the correct spline version, we must study the most widely used splines and select the best one. In the given research, we considered splines for plane curve modeling, as the displacements were determined for point cloud cross-sections. These cross-sections were generated along the ski jump runway. So, the goal is to determine the spline function representing the ski jump cross-section.

In general, spline functions have the following types: interpolation splines, smoothing splines, and regression splines. In what follows, we will study the first two groups. Of course, splines can be classified differently (degree, constraints, basis function, knot distribution, etc.). The essential feature of a spline is the capability to control the curve form locally. After analyzing splines in the dedicated literature [64-67], we have selected the interpolation and approximation spline functions that will be studied. In Table 3, one may find the list of splines, including some of their features. For comparison, we have added the simple interpolation methods.

Table 3. The list of studied splines

Model	Function type	Continuity
Interpolation		
1	Linear Interpolation	C
2	Cubic Interpolation	C
3	Piecewise Cubic Hermite Interpolation	C'
4	Modified Piecewise Cubic Hermite Interpolation	C'
5	Cubic Spline Natural	C''
Approximation		
6	B-spline 1 (n_{knots} equal half of the data set)	C''
7	B-spline 2 (n_{knots} equal maximum allowable value)	C''
8	Least Squares B-spline	C''
9	Smoothing Spline (4 th order)	Can be different
10	Smoothing Spline (6 th order)	Can be different

In Table 3, C determines the level of continuity in spline points. Generally speaking, the condition C means that the spline goes through the interpolation points. The condition C' means that condition C holds, and the first derivative equals at the interpolation points. The condition C'' means that two previous conditions hold, and the second derivative equals at the interpolation points. These conditions ensure the smoothness of splines and prevent high oscillations typical for ordinary high-order interpolation. The listed splines were tested for plane cross-sections of ski jumps that present the observation results for different epochs.

3. Allowable Accuracy Assignment

This section presents the implementation of the procedure suggested for monitoring accuracy calculation. The necessary data for calculation have been obtained in Section 2. Here, we present the developed mathematical models intended to find allowable monitoring accuracy. The allowable monitoring accuracy permits reliably discerning the structure displacements that exceed undesirable or dangerous limit values for this structure. The equation for accuracy determination is given in Shults [47].

$$m_i = \mp t |\delta_i|, \quad (1)$$

where i^{th} subscript corresponds to the load case, δ is a structure deformation acquired by FEM simulation for i^{th} load case, m is monitoring accuracy, t is a reliability coefficient that can accept values in a range of 0.15-0.3, with three standard values of 0.1, 0.15, and 0.2. Typically, $t = 0.1$ is assigned to structures with extremely high safety levels, $t = 0.15$ to high-safety level structures and $t = 0.2$ to structures with a standard safety level. Figure 12 explains the Equation 1. If we observe displacements with allowable accuracy m_i there is only a 10-20% chance that the determined displacement will exceed the simulated value. These limits correspond to reserved structure durability that civil engineers include during the structure design. Therefore, our measurements will detect any abnormal displacements with the necessary reliability. We developed four models for accuracy calculation according to the obtained simulation results.

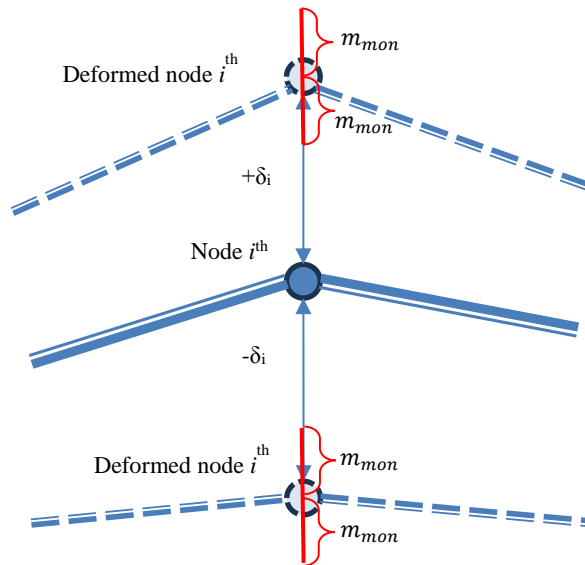


Figure 12. Principle of allowable monitoring accuracy

The first model is named the **min-max model**. In this model, we calculate accuracy for each load case and choose the maximum values of displacements from simulation results along the coordinate axis.

$$\delta_{1x}, \delta_{1y}, \dots, \delta_{iz} \Rightarrow m_{1x}, m_{1y}, \dots, m_{iz}. \tag{2}$$

From all values of accuracy m_i , we choose one that has a minimum value. Thus, the accuracy model will have a simple form

$$m_{mon(Model1)} = m^{min}, \tag{3}$$

where m_{mon} is allowable monitoring accuracy. Monitoring accuracy along the coordinate axis will be

$$m_x^{mon} = t\delta_{ix}, m_y^{mon} = t\delta_{iy}, m_z^{mon} = t\delta_{iz}, \tag{4}$$

where $\delta_{ix}, \delta_{iy}, \delta_{iz}$ are structure deformations acquired by FEM simulation for i^{th} load case along the coordinate axis. This model's drawback is that its accuracy is overestimated because it takes extreme load cases from different combinations, which does not always occur in practice.

The second model is named the **averaged accuracy model**. For this model, we assumed that if the number of loads exceeds four, the displacements from different loads may partly compensate for each other. So, the accuracy is calculated as an average value from obtained displacements for every node

$$m_{mon(Model2)} = \frac{\sum m_i}{i}, \tag{5}$$

where i is the number of load cases.

Tables 4 and 5 present the results of Models 1 and 2 for the ski jumps K95 and K125.

Table 4. Simulated allowable monitoring accuracy for K95

Load case							Min-max model (Model 1)	Averaged accuracy model (Model 2)
1	2	3	4	5	6			
δ_x . m	0.024	0.063	0.027	0.066	0.684	0.348		
δ_y . m	0.068	0.094	0.069	0.095	0.636	0.703		
δ_z . m	0.013	0.037	0.022	0.047	0.353	0.207		
t	0.15							
m_x . m	0.004	0.009	0.004	0.010	0.103	0.052	0.004	0.030
m_y . m	0.010	0.014	0.010	0.014	0.095	0.105	0.010	0.041
m_z . m	0.002	0.006	0.003	0.007	0.053	0.031	0.002	0.017
t	0.2							
m_x . m	0.005	0.013	0.005	0.013	0.137	0.070	0.005	0.041
m_y . m	0.014	0.019	0.014	0.019	0.127	0.141	0.014	0.056
m_z . m	0.003	0.007	0.004	0.009	0.071	0.041	0.003	0.023
t	0.3							
m_x . m	0.007	0.019	0.008	0.020	0.205	0.104	0.007	0.061
m_y . m	0.020	0.028	0.021	0.029	0.191	0.211	0.020	0.083
m_z . m	0.004	0.011	0.007	0.014	0.106	0.062	0.004	0.034

Table 5. Simulated allowable monitoring accuracy for K125

Load case							Min-max model (Model 1)	Averaged accuracy model (Model2)
1	2	3	4	5	6			
δ_x . m	0.026	0.065	0.543	0.535	2.798	2.807		
δ_y . m	0.094	0.115	0.111	0.133	0.349	0.349		
δ_z . m	0.023	0.04	0.599	0.589	1.878	1.874		
t	0.15							
m_x . m	0.004	0.010	0.081	0.080	0.420	0.421	0.004	0.169
m_y . m	0.014	0.017	0.017	0.020	0.052	0.052	0.014	0.029
m_z . m	0.003	0.006	0.090	0.088	0.282	0.281	0.003	0.125
t	0.2							
m_x . m	0.005	0.013	0.109	0.107	0.560	0.561	0.005	0.226
m_y . m	0.019	0.023	0.022	0.027	0.070	0.070	0.019	0.039
m_z . m	0.005	0.008	0.120	0.118	0.376	0.375	0.005	0.167
t	0.3							
m_x . m	0.008	0.020	0.163	0.161	0.839	0.842	0.008	0.339
m_y . m	0.028	0.035	0.033	0.040	0.105	0.105	0.028	0.058
m_z . m	0.007	0.012	0.180	0.177	0.563	0.562	0.007	0.250

Despite better efficiency, this model does not account for the fact that displacements may have different signs. Therefore, the third model is named the **absolute accuracy model**. In this model, we first calculate the mean absolute displacement for the whole structure

$$\bar{\delta}_t = \frac{\sum |\delta_n|}{n}, \tag{6}$$

where n is the number of nodes.

Then, for every load case, we determine the allowable monitoring accuracy

$$m_{mon(Model3)} = t\bar{\delta}_t. \tag{7}$$

The fourth model (**averaged absolute accuracy model**) is similar to model two but operates with absolute displacements.

$$m_{mon(Model4)} = \frac{\sum \bar{m}_i}{i}. \tag{8}$$

Tables 6 and 7 present the results of Models 3 and 4 for the ski jumps K95 and K125.

Table 6. Simulated allowable monitoring accuracy for K95

Load case							Absolute accuracy model (Model 3)	Averaged absolute accuracy model (Model 4)
1	2	3	4	5	6			
δ_x . m	0.013	0.033	0.013	0.032	0.244	0.120		
δ_y . m	0.057	0.080	0.057	0.080	0.265	0.406		
δ_z . m	0.005	0.012	0.010	0.017	0.161	0.077		
t	0.15							
m_x . m	0.002	0.005	0.002	0.005	0.037	0.018	0.002	0.012
m_y . m	0.009	0.012	0.009	0.012	0.040	0.061	0.009	0.024
m_z . m	0.001	0.002	0.002	0.003	0.024	0.012	0.001	0.007
t	0.2							
m_x . m	0.003	0.007	0.003	0.006	0.049	0.024	0.003	0.015
m_y . m	0.011	0.016	0.011	0.016	0.053	0.081	0.011	0.031
m_z . m	0.001	0.002	0.002	0.003	0.032	0.015	0.001	0.009
t	0.3							
m_x . m	0.004	0.010	0.004	0.010	0.073	0.036	0.004	0.023
m_y . m	0.017	0.024	0.017	0.024	0.080	0.122	0.017	0.047
m_z . m	0.002	0.004	0.003	0.005	0.048	0.023	0.002	0.014

Table 7. Simulated allowable monitoring accuracy for K125

Load case							Absolute accuracy model (Model 3)	Averaged absolute accuracy model (Model 4)
1	2	3	4	5	6			
δ_x . m	0.010	0.023	0.121	0.128	0.504	0.114		
δ_y . m	0.032	0.040	0.033	0.041	0.072	0.086		
δ_z . m	0.007	0.015	0.098	0.099	0.329	0.065		
t	0.15							
m_x . m	0.002	0.003	0.018	0.019	0.076	0.017	0.002	0.023
m_y . m	0.005	0.006	0.005	0.006	0.011	0.013	0.005	0.008
m_z . m	0.001	0.002	0.015	0.015	0.049	0.010	0.001	0.015
t	0.2							
m_x . m	0.002	0.005	0.024	0.026	0.101	0.023	0.002	0.030
m_y . m	0.006	0.008	0.007	0.008	0.014	0.017	0.006	0.010
m_z . m	0.001	0.003	0.020	0.020	0.066	0.013	0.001	0.021
t	0.3							
m_x . m	0.003	0.007	0.036	0.038	0.151	0.034	0.003	0.045
m_y . m	0.010	0.012	0.010	0.012	0.022	0.026	0.010	0.015
m_z . m	0.002	0.005	0.029	0.030	0.099	0.020	0.002	0.031

Results from Tables 4 to 7 can be easily presented in charts (Figures 13 and 14).

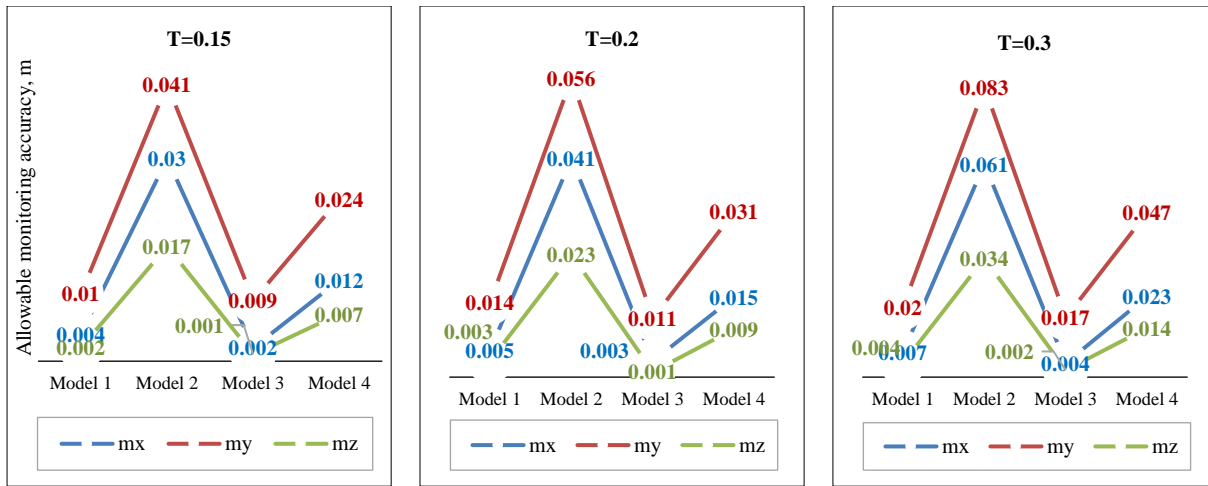


Figure 13. Charts of allowable monitoring accuracy for K95

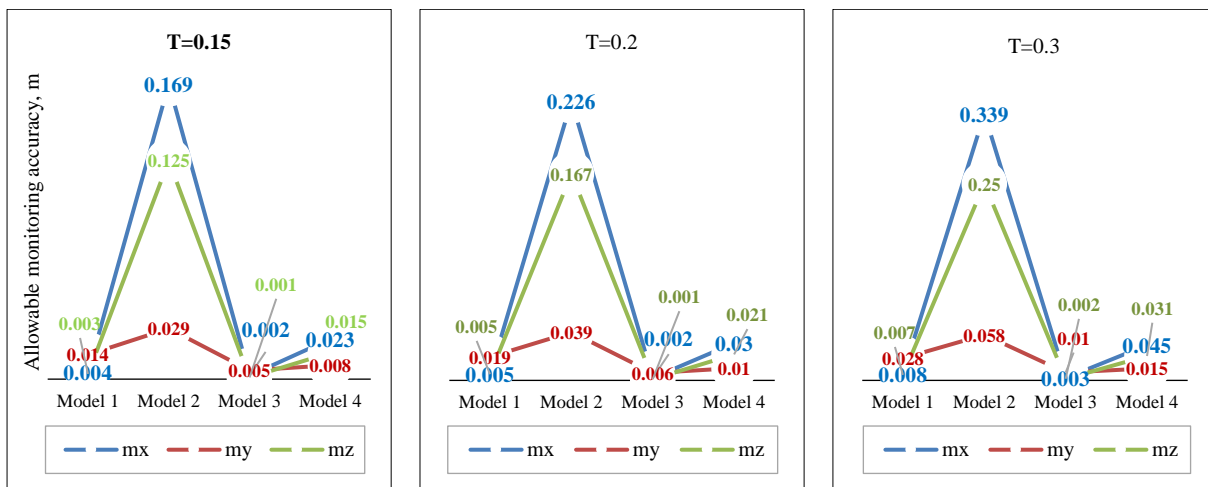


Figure 14. Charts of allowable monitoring accuracy for K125

The considered models present different results. However, from Tables 4 to 7 and Figures 13 and 14, one may notice some general tendencies. If we assume that ski jumps have a high safety level, then we apply a reliability coefficient of 0.15. The ski jump K125 has a larger size and more significant displacements consequently. This structure is more massive and durable and can undergo larger loads. Therefore, it is recommended to assign allowable accuracy with a smaller value to avoid the different monitoring accuracy for different ski jumps. Such an approach guarantees that significant displacements will be determined confidently for both ski jumps. Thus, we apply the accuracy of basic monitoring related to ski jump K95 monitoring. The next step is to choose the accuracy model. Since the ski jumps are subject to multiple loads, we recommend selecting averaged accuracy or averaged absolute accuracy models. Based on simulation results, the following monitoring accuracy has been assigned along the coordinate axis: $m_x = 0.041$ m, $m_y = 0.030$ m, $m_z = 0.017$ m. So, the first goal of the paper declared the method and algorithm development for the assignment of allowable monitoring accuracy using FEM simulation results is achieved. The obtained accuracy distribution reflects the nature of structure deformation. The X-axis coincides with the longitudinal axis of ski jumps. Thus, the displacements along this axis are essential (lower accuracy). Lateral (Y-axis) and vertical (Z-axis) displacements are smaller, with higher accuracy. As was mentioned in the introduction, the primary stress of the monitoring is concentrated on vertical displacements, which need the highest accuracy.

4. Results and Discussion

4.1. Geodetic Network Design and Creation

The determined allowable accuracy was used for geodetic network design. It is believed that network accuracy must be at least three times higher than allowable monitoring accuracy [47] to neglect the influence of errors in the geodetic network. The highest accuracy of coordinate determination must be ensured for vertical displacements, $m_z = 0.017$ m. Thus, the network accuracy should be between ± 5 -10 mm along the different coordinate axes. In particular, it must be equal or higher ± 5 mm for vertical displacements. Such accuracy can be achieved using state-of-the-art geodetic equipment. Scanning total station Leica Nova MS60A combines total station and terrestrial laser scanner functions. The accuracy of the total station according to its specification is more than sufficient to ensure network and observation

accuracy. The total station used was certified by Leica Geosystems. A geodetic network was created in a local coordinate system with two initial points (1000 and 1001), with point 1000 as a point of beginning. The criterion for network point selection was their stability. Since there are only two stable areas, we placed points on the top of the ski jump and at the bottom. The scheme of the geodetic network is presented in Figure 15. After measurements, the network was adjusted, and the point accuracy was estimated. Network accuracy is presented using error ellipses with a confidence level of 95%. The network scheme with absolute and relative ellipses is given in Figure 15.

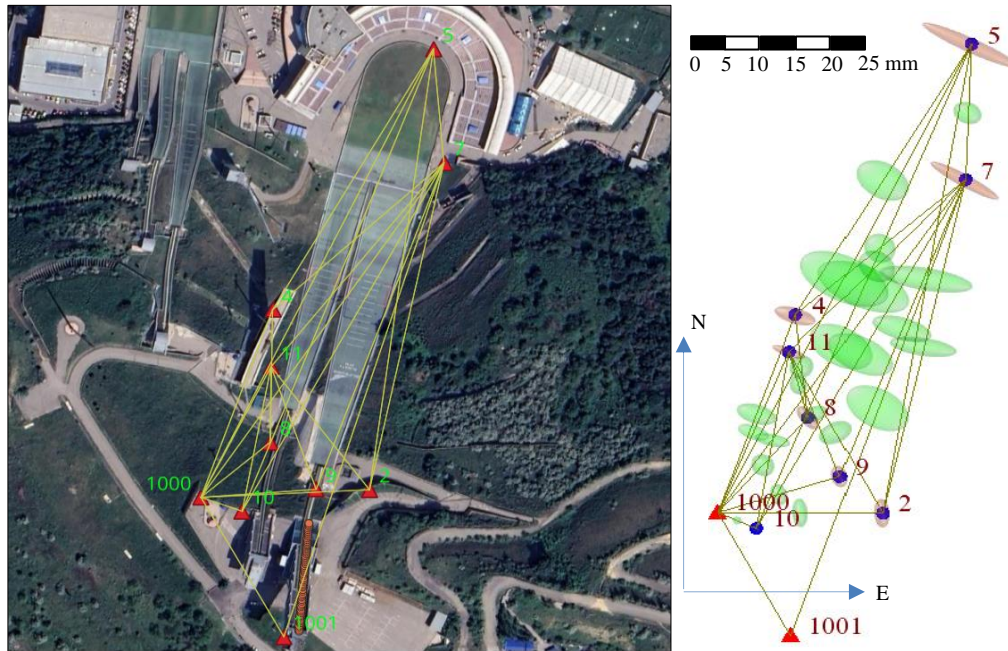


Figure 15. Scheme of monitoring network

The estimated accuracy of the network may be found in Table 8.

Table 8. Accuracy of monitoring network

Point number	Parameters of error ellipses for confidence probability 95%				Point accuracy, m		
	Semi-major axis, m	Semi-minor axis, m	Azimuth of major axis, deg	Vertical axis, m	N	E	Z
2	0.0044	0.0022	176	0.0030	0.0009	0.0018	0.0015
4	0.0060	0.0024	107	0.0020	0.0023	0.0012	0.0010
5	0.0149	0.0022	116	0.0022	0.0055	0.0028	0.0011
7	0.0110	0.0018	120	0.0019	0.0039	0.0024	0.0010
8	0.0041	0.0021	143	0.0027	0.0012	0.0014	0.0014
9	0.0033	0.0022	166	0.0023	0.0010	0.0013	0.0012
10	0.0012	0.0011	117	0.0013	0.0005	0.0005	0.0007
11	0.0049	0.0014	108	0.0013	0.0019	0.0009	0.0007

Considering the confidence level of 95% (the estimated accuracy is doubled), we may conclude that the yielded accuracy of point coordinates does not exceed 3 mm. Such accuracy will ensure undistorted values of displacements throughout monitoring.

4.2. Monitoring Results

We have design coordinates for both ski jumps along the longitudinal axis. These coordinates are accepted errorless and treated as zero observation epochs for subsequent comparison with the following observation epochs. The first observation epoch was carried out in August 2021. The total station was georeferenced using the free station method at each scanning station. Thanks to that, the final point cloud was already referenced to the accepted coordinate system (Figure 16-a). An additional adjustment was made using artificial objects identified in overlaps between clouds. In total, scanning was accomplished from seven points. After referencing, the point cloud was filtered out of unnecessary artifacts and blunders. The final point cloud of two ski jumps is presented in Figure 16-b. The point cloud size after filtering equals half a million points. A similar point cloud was generated after the second observation epoch in August 2022.

The longitudinal cross-sections of the ski jump surface were obtained to determine the vertical displacements for each point cloud. The sample of such a cross-section for landing hill K125 is portrayed in Figure 17.

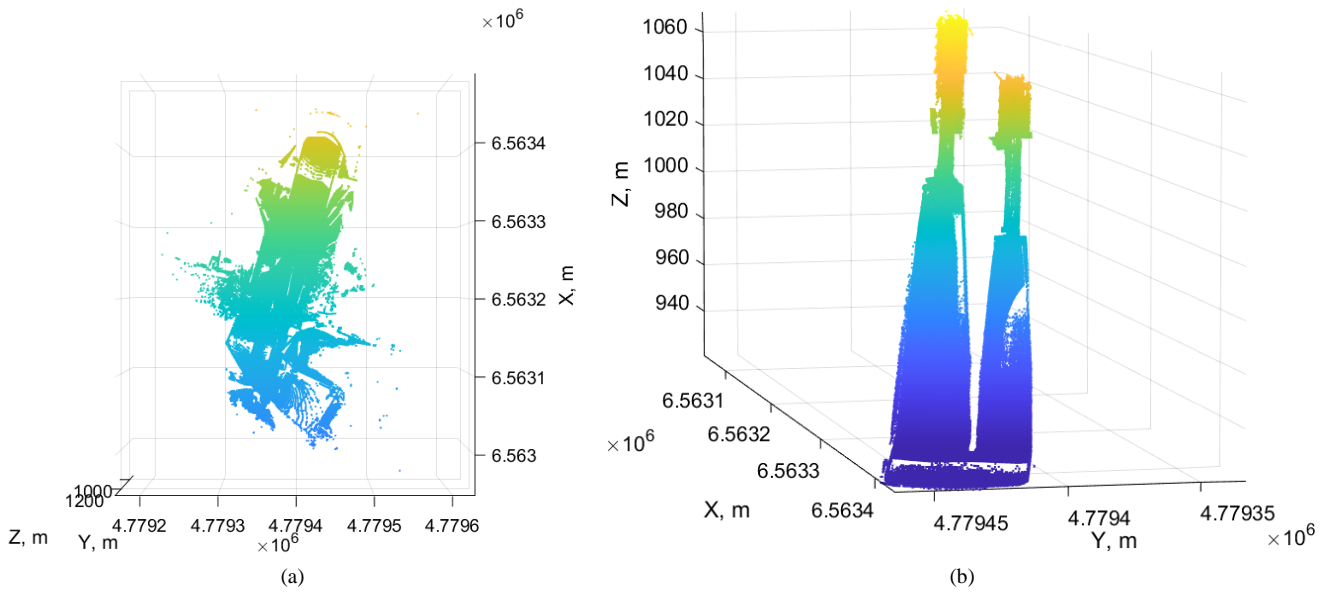


Figure 16. Georeferenced point cloud for two ski jumps: a) top view of unfiltered cloud, b) 3D view of filtered point cloud

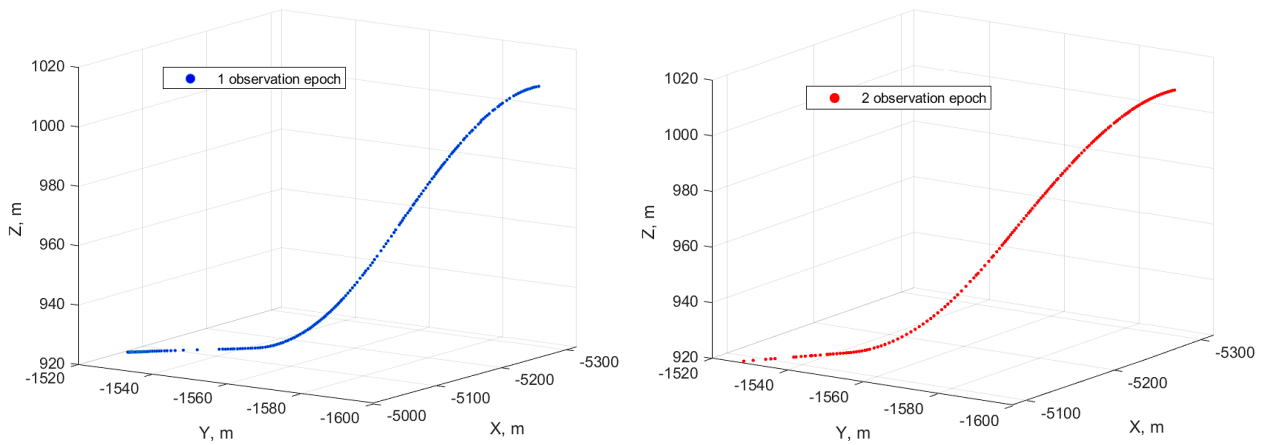


Figure 17. Cross-sections for two observation epochs, landing hill of ski jump K125

Figure 17 confirms the fact that cross-sections of different epochs have a distinct number of points with different spacing between them. This discrepancy is related to different scanner orientations. For precise verification, let us overlay and zoom in on two observation epochs for the runway ramp of ski jump K125 (Figure 18).

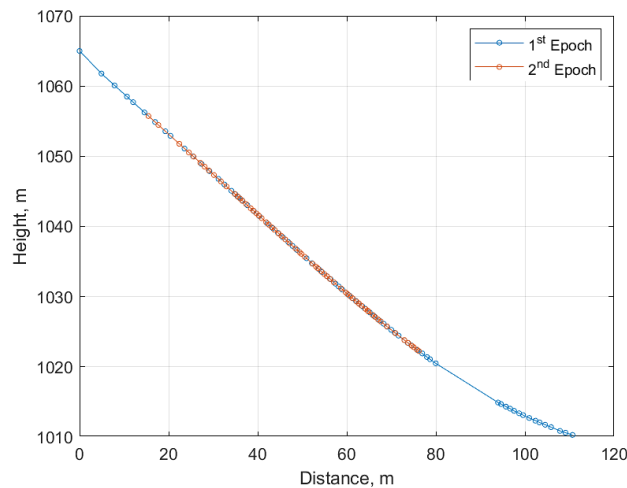


Figure 18. Runway ramp of ski jump K125

The difference between the two cross-sections is significant. Thus, it is impossible to compare different epochs until the cross-sections are interpolated and transformed into uniformly spaced points. This is why the second goal of the paper is to investigate different spline functions for displacement simulation and analysis.

4.3. Spline Simulation Results

The simulation task is intended to provide answers to two questions. First, which accuracy is achievable for spline interpolation/approximation? Second, which spline form will ensure the best interpolation/approximation accuracy? We want to note that despite the difference between interpolation and approximation, in our case, we deal only with spline functions, so both definitions are used interchangeably. To address the first question, we tested all data sets using spline functions listed in Table 3. For each observation epoch, the points in a cross-section were split into two subsamples: training and testing. The relationship between the training and testing subsamples was accepted 75/25. Therefore, we used 75% of the points for spline construction and then checked the deviations of this spline for reserved testing points. As a result, the discrepancies between interpolated and observed values were calculated. By these discrepancies, the interpolation accuracy was estimated using root mean square errors (RMS). In order to have the allowable value for interpolation or approximation accuracy m_{inter} , we may use the theoretical network accuracy $m_{net} = 5$ mm, total station accuracy from specification $m_{ts} = 2$ mm, and monitoring accuracy for vertical displacements $m_Z = 17$ mm. Thus, we will have

$$m_{int} = \sqrt{m_Z^2 - m_{ts}^2 - m_{net}^2} \tag{9}$$

The expression 9 gives the allowable interpolation accuracy $m_{int} = 16$ mm. It is necessary to note that the absolute values of the RMS errors have no meaning. Because displacements distort the interpolated values, the interpolation model accuracy can be used only for relative comparison with other models. The primary purpose is to determine the lower RMS error value for the selected data set. This lower value indicates the model that ensures the best interpolation, not the accuracy of displacement determination.

Below, we present the charts of the differences between interpolated and testing points for the runway ramp of the ski jump K125. The discrepancies are grouped in three charts (Figure 19) for convenience.

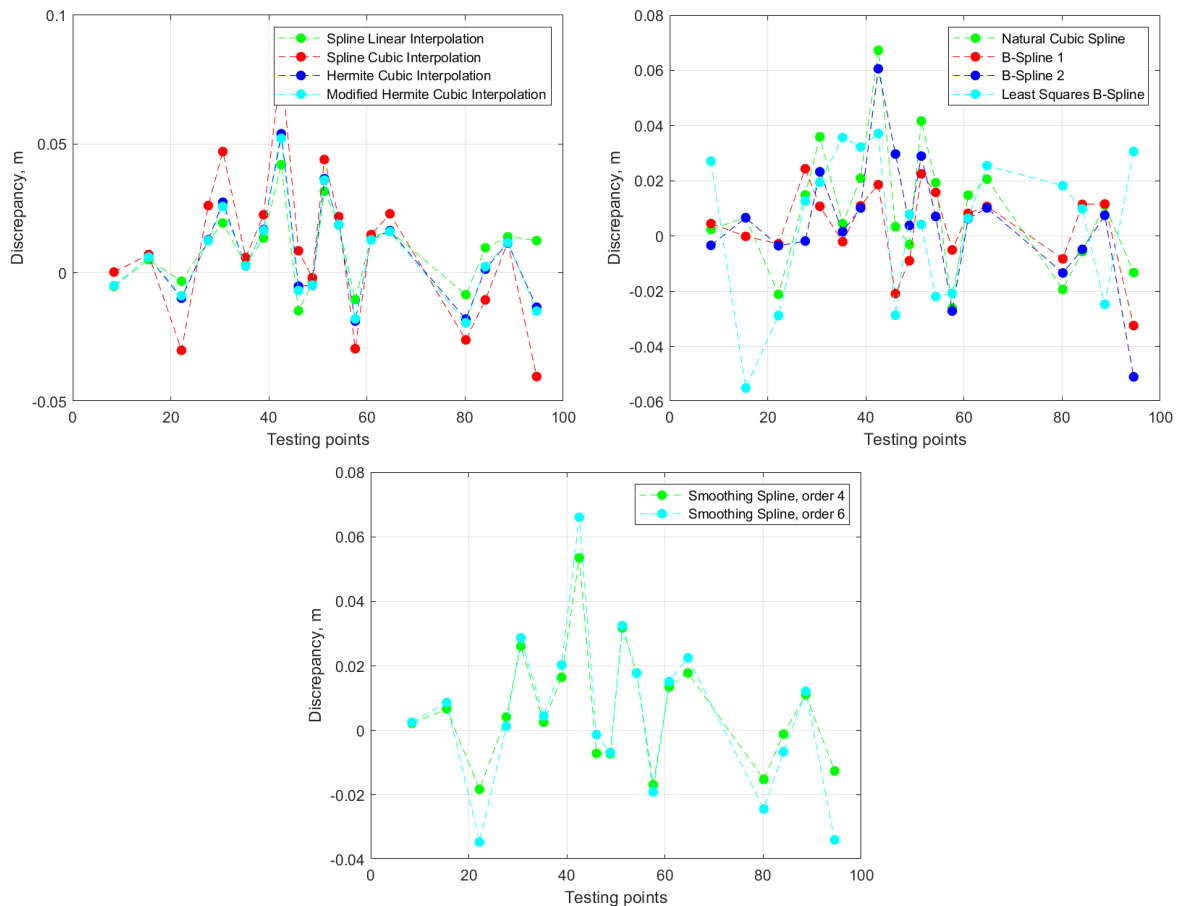


Figure 19. Charts of deviations for testing points (first epoch) for different spline functions, ski-jump K125

Similarly, testing was accomplished for all observation epochs for both ski jumps. After each simulation, the accuracy estimations were determined. The simulation results are summarized in Table 9.

Table 9. Estimations of interpolation/approximation accuracy for different spline functions (models)

Model	RMS, m					
	K125 runway ramp		K125 landing hill		K95 landing hill	
	Epoch 1	Epoch 2	Epoch 1	Epoch 2	Epoch 1	Epoch 2
Model 1	0.014	0.006	0.024	0.035	0.013	0.011
Model 2	0.030	0.006	0.034	0.044	0.017	0.013
Model 3	0.019	0.006	0.024	0.036	0.011	0.010
Model 4	0.018	0.006	0.024	0.035	0.011	0.010
Model 5	0.023	0.006	0.027	0.039	0.013	0.012
Model 6	0.014	0.007	0.021	0.035	0.011	0.014
Model 7	0.023	0.008	0.049	0.043	0.017	0.014
Model 8	0.027	0.006	0.022	0.026	0.010	0.014
Model 9	0.018	0.007	0.026	0.038	0.011	0.010
Model 10	0.024	0.007	0.033	0.041	0.014	0.011

The results in Table 9 can be easily visualized. In Figure 20, we present the charts of simulation accuracy distribution for different models regarding the observation epoch and ski jumps.

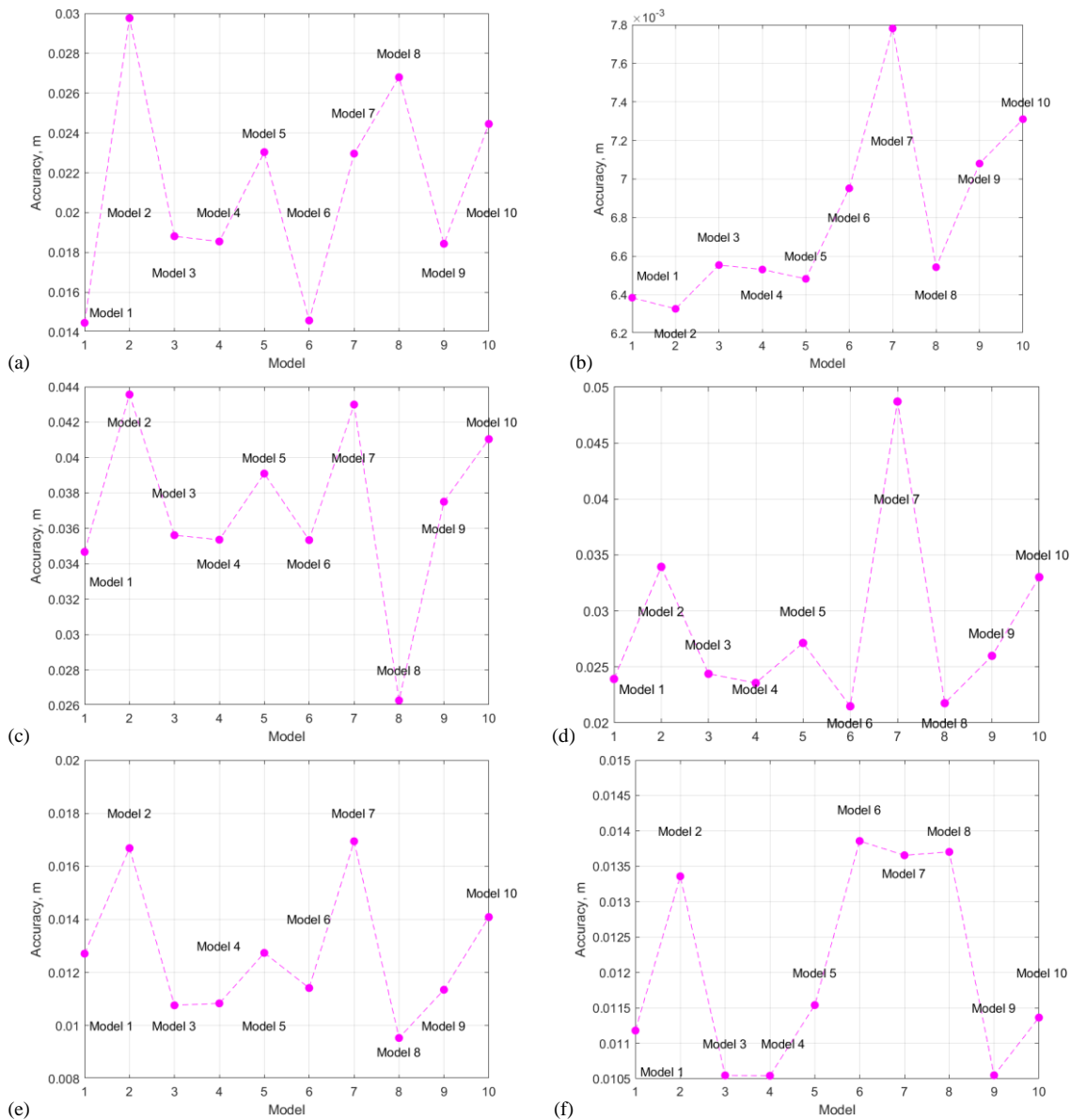


Figure 20. Accuracy estimations for spline interpolation/approximation for: a) first observation epoch for the runway ramp of ski jump K125, b) second observation epoch for the runway ramp of ski jump K125, c) first observation epoch for the landing hill of ski jump K125, d) second observation epoch for the landing hill of ski jump K125, e) first observation epoch for the landing hill of ski jump K95, f) second observation epoch for the landing hill of ski jump K95.

The values of the RMS errors range from 0.006 m to 0.049 m. The first case requires special attention (Figure 20-a). The best accuracy provides a B-spline approximation built on a knot number equal to half the data set and, surprisingly, simple linear interpolation. The reason for significant RMS errors is a gap in data in the lower part of the runway ramp of K125. The graphs in Figure 21-a confirm this issue. Figure 21-b presents the zoomed part with the data gap. One may see that interpolated values significantly deviate once the distance between measured points exceeds 10 m.

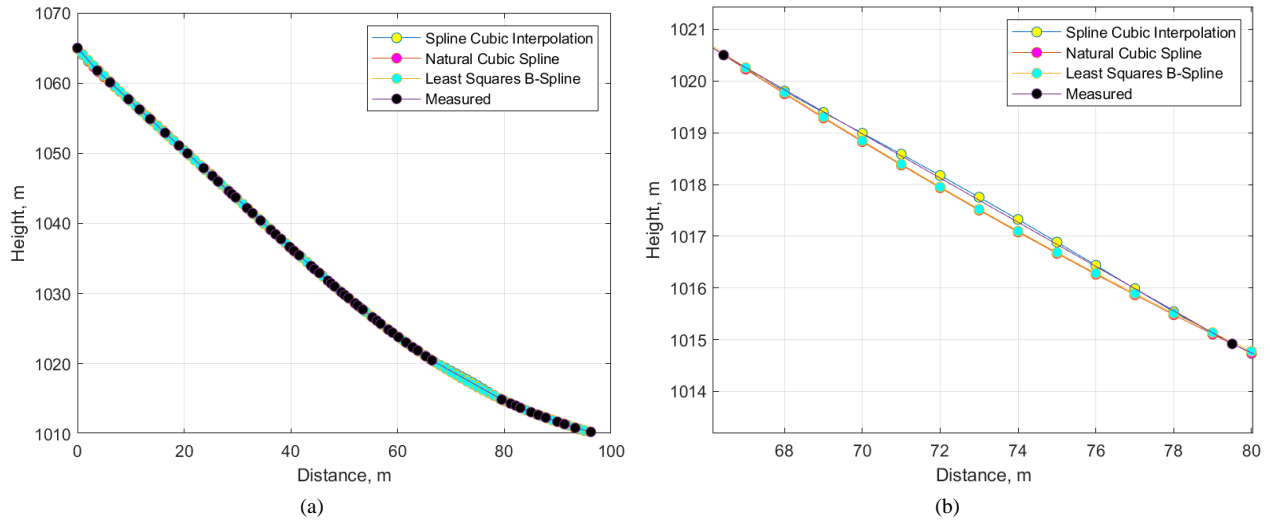


Figure 21. Measured points and data gap for runway ramp K125: a) measured points and interpolation curves, b) zoomed part with data gap

The interpolation models provide different outputs for the second observation epoch of the same runway ramp of K125. However, all the analyzed models have accuracy ranging from 0.006 to 0.008 m, which is considerably better than the necessary displacement accuracy determination. Therefore, we can apply any of the models without loss of accuracy. Summing up the results, we recommend using a B-spline approximation built on a knot number equal to half the data set.

The simulation results for the landing hill of K125 are similar for both epochs. The better spline functions are the same as in the previous case. The best accuracy for the first observation epoch is achieved using the model based on the least squares B-spline. The data set generated in the second observation epoch is better interpolated using least squares B-spline and B-spline approximation built on a knot number equal to half the data set. Therefore, the best interpolation/approximation solution for the landing hill of K125 is the usage of least squares B-spline.

Spline functions built on the data for the landing hill of K95 provide very close results. The RMS errors fluctuate in the range of 0.010-0.017 m. Such accuracy is enough for displacement analysis. The least squares B-spline has better accuracy for the first observation epoch. For the second epoch, better accuracy is achieved through the piecewise cubic Hermite spline, modified piecewise cubic Hermite spline, and smoothing spline. Yet the accuracy for the whole model set fluctuates around 4 mm. Thus, we can recommend the usage of least squares B-spline.

The results may raise questions about spline function efficiency. To prove our choice in favor of least squares B-splines, let us consider the most popular approximation models in geodesy, namely polynomial regression and Fourier series. We tested two models with a large number of coefficients: polynomial regression of 9th degree Equation 10 and Fourier series with eight terms (Equation 11):

$$h_i = a_0 + a_1x_i + a_2x_i^2 + \dots + a_9x_i^9, \tag{10}$$

$$h_i = a_0 + a_1 \cos \omega x_i + b_1 \sin \omega x_i + a_2 \cos \omega x_i + b_2 \sin \omega x_i + \dots + a_9 \cos \omega x_i + b_9 \sin \omega x_i, \tag{11}$$

where a_0 is a constant (intercept) coefficient, ω is the fundamental frequency of the signal, x_i is an observation point.

These models were tested on the same observations of the landing hill of K125 and divided into training and testing subsamples. Results for polynomial regression are given in Figure 22 and for Fourier series in Figure 23. For polynomial regression, the RMS error on the training subsample equals 0.031 m. For the testing subsample, the RMS error equals 0.051 m. Such accuracy is three times bigger than the allowable value $m_{int} = 16 \text{ mm} < 51 \text{ mm}$. Fourier series ensure better accuracy, with training RMS error equals 0.029 m and testing RMS error 0.027 m. However, it is still more significant than the allowable value.

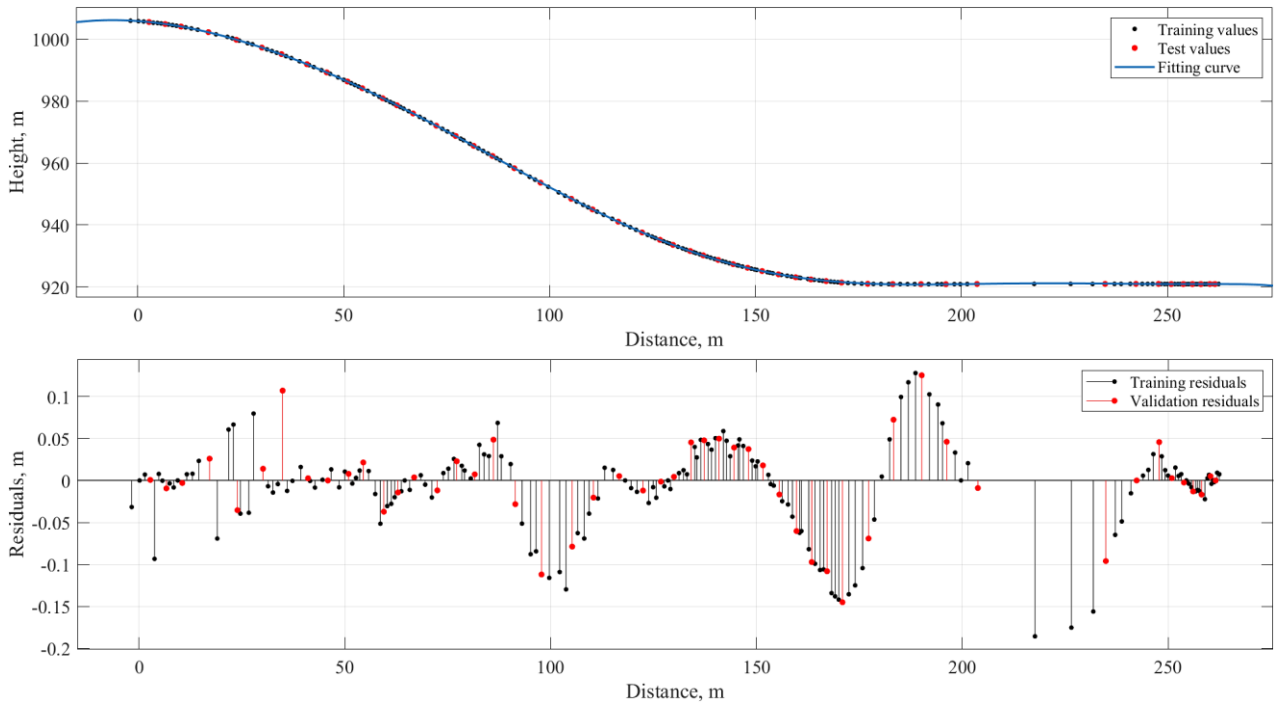


Figure 22. Polynomial regression approximation and residuals, landing hill K125

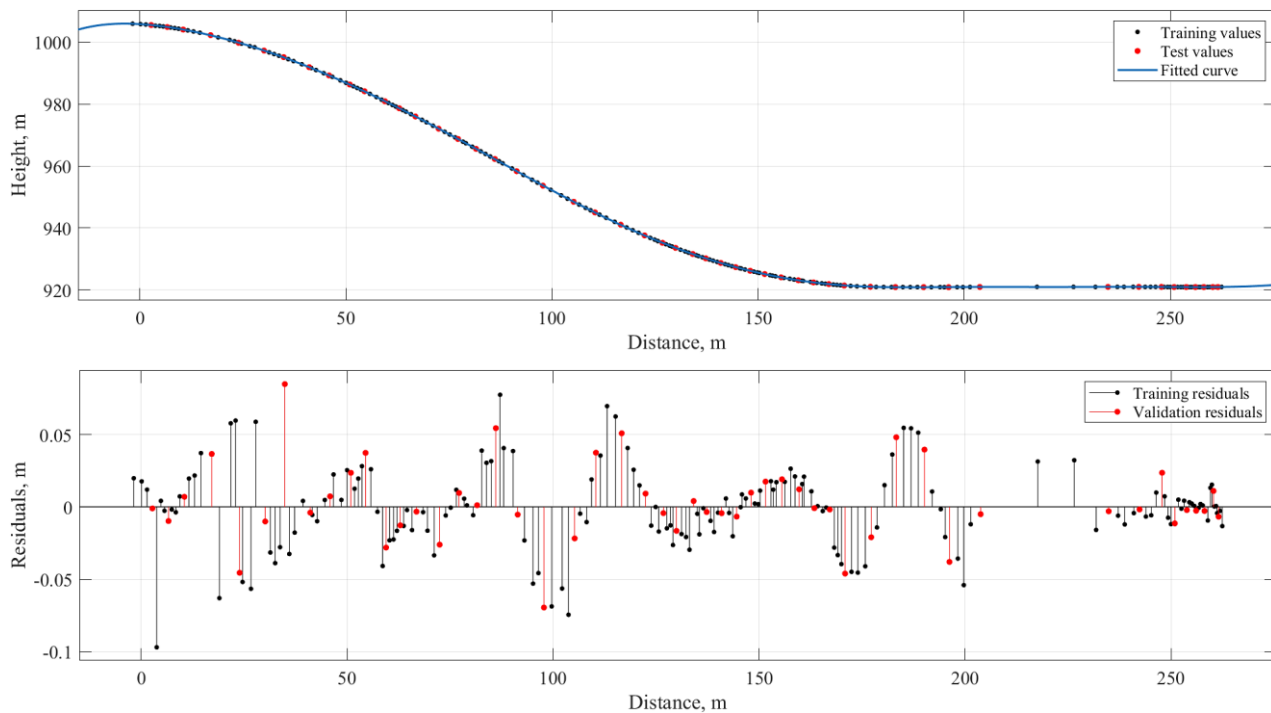


Figure 23. Fourier series approximation and residuals, landing hill K125

As in previous studies [51-53], the results of our research confirm that B-splines are suitable solutions for TLS data simulation. In contradiction to [56-58], where the B-spline application is taken for granted, we obtained a quantitative estimation that proves the efficiency of this class of functions. So, B-splines have significant flexibility and provide the necessary interpolation accuracy. The general picture emerging from the analysis is that various B-splines allow precisely simulating structures with complex geometry. We suggest applying the least squares B-splines for the runway ramp of K125 and the landing hill of K95. B-spline approximation built on a knot number equal to half the data set is the best for the landing hill of K125. Once the best spline function was chosen, the simulation procedure was repeated for the whole data set (training plus testing). The final spline function was used for uniform interpolating of measurement results and displacement analysis.

4.4. Displacement Analysis

The final stage is the displacement analysis using the suggested spline function. We can calculate equally spaced points since we have spline functions that precisely describe the measurements at each observation epoch. This uniformity is necessary to compare measurement results with each other and with the design curve, which is specified by coordinates with 1-meter intervals. Thus, we can calculate displacements regarding the design curve. Figure 24 illustrates this approach.

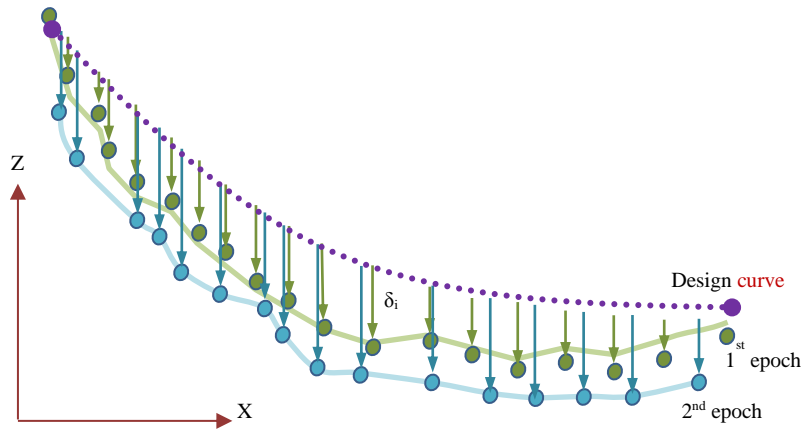


Figure 24. The correspondence between the design curve and observations

In the previous subsection, we determined the best spline models with the highest interpolation accuracy for each observation epoch. It allows us to proceed to displacement determination and analysis.

Firstly, we analyzed the displacements of the runway ramp of the ski jump K125. For the analysis, we used the least squares B-spline built on three optimal knots for the first epoch and four knots for the second epoch. In Figure 25, one may see the displacements that occurred between the first and second observation epochs.

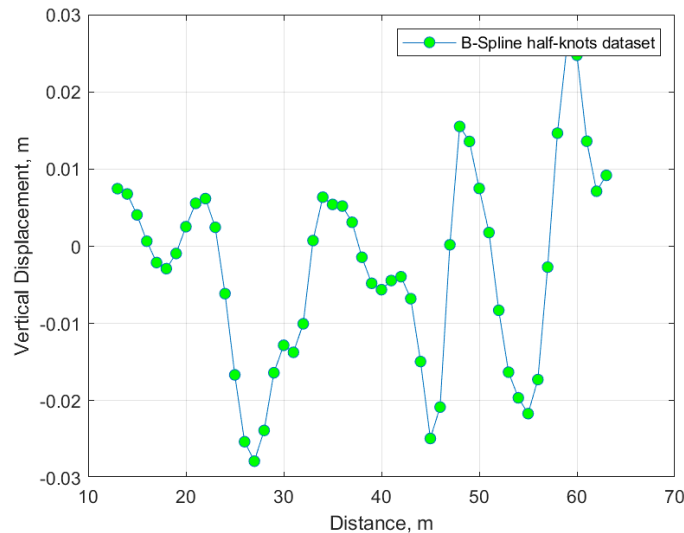


Figure 25. Displacement chart for the runway ramp of the ski jump K125

The graph in Figure 25 demonstrates the periodic nature of the displacements. The waves have a maximum amplitude of 40 mm with a slight uplift in the lower part of the ramp. The negative displacements reached -30 mm with a wavelength of around 10 m. The positive displacements correlate with the displacements of the landing hill, as will be seen below. Now, let us analyze the displacements for the landing hill of K125. The interpolation was accomplished by B-splines with a number of knots depending on the size of the data sets (100 knots for the first epoch and 75 knots for the second epoch). The appropriate graph is given in Figure 26.

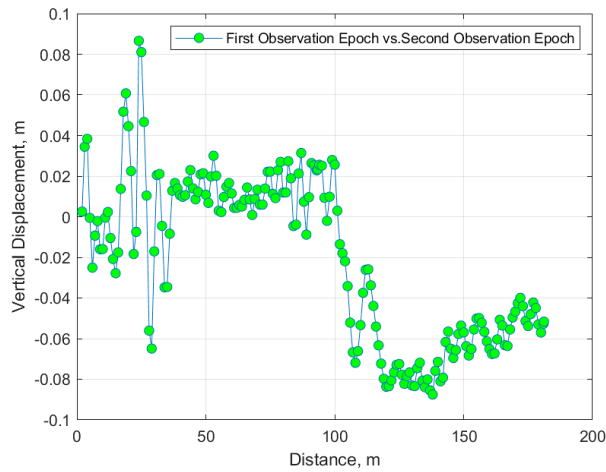


Figure 26. Displacement chart for the landing hill of the ski jump K125

For these data, we could employ B-spline or least squares B-spline. To show the fine quality of both spline functions, we overlaid them in one chart (Figure 27). The comparison reveals no significant difference between these models. However, the least squares B-spline exhibits more significant fluctuations. Analyzing Figure 28, one may conclude that the upper part of the landing hill has a minor uplift (20 mm on average), corresponding to the previous results for the runway ramp. The landing hill has negative average displacements of 60 mm starting from a distance of 100 m. Of interest is a comparison of different observation epochs with design values. Figure 28 presents such a comparison. The obtained results show the discrepancies between observations and design values. However, these differences demonstrate the construction imperfections determined after the first observation epoch. At this stage, the displacements and the construction imperfections are mixed, and it is impossible to tell them apart. The displacements become identifiable only beginning with the second observation epoch. Anyway, in Figure 28, we can also examine the differences that become significant starting from a distance of 100 m.

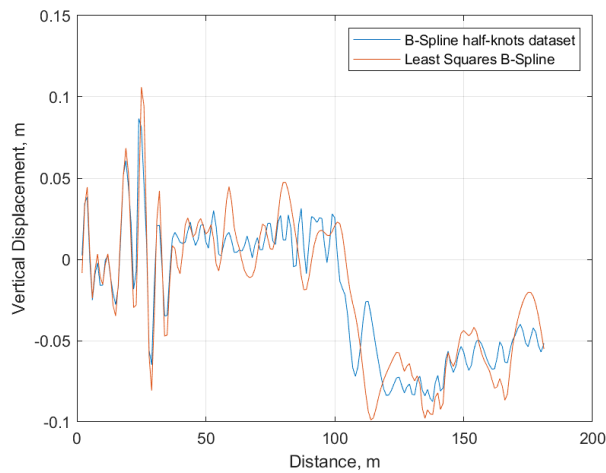


Figure 27. Comparison between B-spline and least squares B-spline interpolation for the landing hill of K125

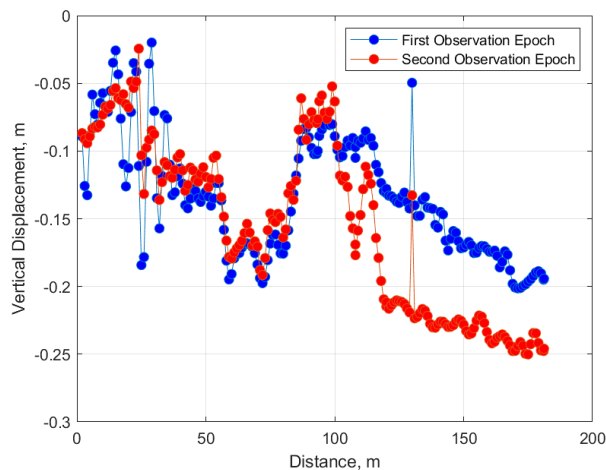


Figure 28. Comparison of different observation epochs and design values for the landing hill of K125

Finally, let us determine the displacements for the landing hill of ski jump K95. For the analysis, we used the least squares B-spline, built on 29 optimal knots for the first epoch and 17 knots for the second epoch. The displacements between the first and second observation epochs are shown in Figure 29.

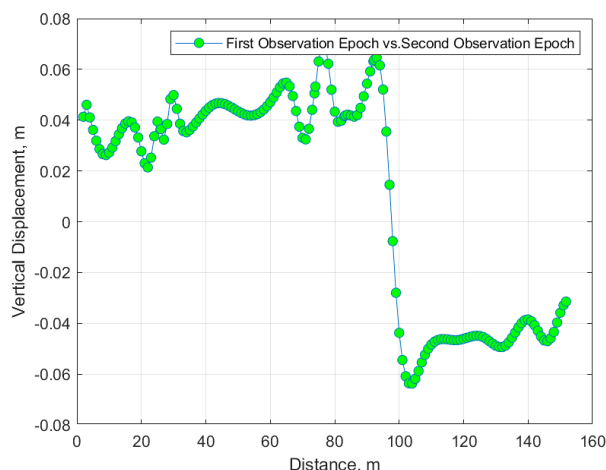


Figure 29. Displacement chart for the landing hill of the ski jump K95

Similarly to the neighbor ski jump K125, this landing hill has an average uplift of 40 mm in the upper part and settlement around -60 mm at the bottom. Let us compare the two observation epochs with design values. The comparison is given in Figure 30.

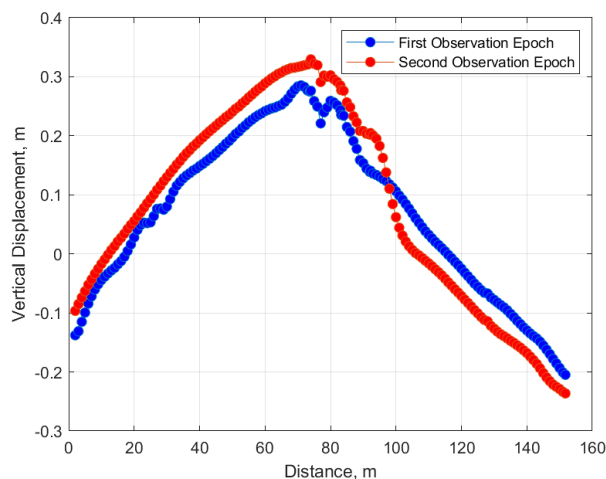


Figure 30. Comparison of different observation epochs and design values for the landing hill of K95

The comparison with design values demonstrates a slightly different displacement distribution. Fig. 30 shows that during construction, the central part of the landing hill departed from the design curve to the value of 0.3 m. Yet this deviation changes slowly and cannot affect the structure exploitation. Nonetheless, the general deformation evolves in the same way as for the ski jump K125. The evident explanation is landslide activity at the bottom of the hill. Unlike the publications [51, 53, 54], where the analysis was done for one observation epoch, we presented the workflow for multitemporal analysis. Similarly to the idea given in [41, 45, 51], at the first stage, we compared a design model and a deformed model from the first observation epoch. This comparison shows instead construction imperfections rather than real deformations. If we now turn to the second observation epoch, then further analysis shows that the surfaces of ski jumps have undergone deformations.

The structural analysis that was performed helped us estimate the structures' operational conditions. Using structural simulation results in Tables 1 and 2, we may infer that for the ski jump K95, maximum theoretical vertical displacement takes place for full load, including dead weight, snow, wind gusts, and hill movement. This displacement reaches 248 mm. After the second observation epoch, the determined displacements have a maximum value of 60 mm, so the structure operates in the allowable range. Regarding ski jump K125, this one has a maximum simulated displacement equal to 109 mm for load case 4, while the observed displacement has a similar value – 60 mm. A comparison of the two results reveals deformations that have no impact on structure exploitation. However, it can be seen that for both ski jumps, the deformation values tend to grow between observation epochs. Therefore, the observations must be expanded to simultaneously monitor the structures and the hill surface.

5. Conclusion

The general idea of the article is to explore the procedure of design and analysis of geodetic monitoring results for massive sports structures. The presented study considers the capabilities of terrestrial laser scanning as measuring equipment for monitoring. As a case study, the ski jump sports complex was selected. For such an object, we developed and described the monitoring workflow and presented the monitoring flowchart. Qualitative geodetic monitoring is only possible with proper accuracy assignment. To reach this goal, we worked out the method that uses the results of the FEM simulation. The paper provides the results of the FEM simulation for two ski jumps. The given simulations included the effect of different loads. The obtained results procured the displacements used further to assign allowable monitoring accuracy. The authors suggested four alternative accuracy models: min-max model, averaged accuracy model, absolute accuracy model, and averaged absolute accuracy model. Based on the model analysis, we recommend using averaged accuracy or averaged absolute accuracy models. The geodetic network project and its adjustment were accomplished using the acquired accuracy. The a posteriori accuracy of the geodetic network was in a range of ± 3 mm. Terrestrial laser scanning was carried out from the points of the geodetic network.

The obtained point clouds were georeferenced and filtered. For displacement analysis, we built cross-sections along the longitudinal axis. To compare these cross-sections for various observation epochs, we tested the different interpolation/approximation functions. The complete list of the tested functions included linear interpolation, cubic interpolation, piecewise cubic Hermite interpolation, modified piecewise cubic Hermite interpolation, cubic natural spline, B-spline with different numbers of knots, least squares B-spline, smoothing spline (4th and 6th order). The best function was selected for each observation epoch. B-splines and least squares B-splines demonstrated the best results. These spline functions were used for interpolation and displacement analysis. The displacement analysis showcased moderate deformations of around 20 mm for the runway ramp of K125. The landing hills for both ski jumps demonstrated more significant displacements of around 60 mm, which is allowable for such structures. In light of the presented study, few conclusions can be drawn. The FEM simulation guarantees reliable input data for monitoring accuracy assignments. The suggested models for accuracy assignment allow us to consider various structure exploitation cases and design geodetic monitoring properly. Spline functions proved useful for displacement analysis. The study affirms the high efficiency of the suggested method and approach for displacement analysis. Our research was limited to one particular structure, so these findings are not generalizable beyond that structure. It is recommended that similar studies be conducted on another massive structure. Future research will have to confirm whether the developed methods and algorithms are applicable to other structure monitoring.

6. Declarations

6.1. Author Contributions

Conceptualization, R.S. and G.S.; methodology, R.S. and G.S.; software, R.S., G.S., and A.A.; validation, R.S., R.D., and A.A.; formal analysis, R.S., A.A., R.D., and S.S.; investigation, R.S., G.S., A.A., S.S., Z.K., and G.O.; resources, G.S., S.S., Z.K., and G.O.; data curation, R.S., G.S., and Z.K.; writing—original draft preparation, R.S.; writing—review and editing, G.S., A.A., and R.D.; visualization, R.S., G.S., and S.S.; supervision, R.S. and G.S.; project administration, R.S., G.S., S.S., and Z.K.; funding acquisition, G.S. All authors have read and agreed to the published version of the manuscript.

6.2. Data Availability Statement

The data presented in this study are available on request from the corresponding author.

6.3. Funding

The authors received no financial support for the research, authorship, and/or publication of this article.

6.4. Conflicts of Interest

The authors declare no conflict of interest.

7. References

- [1] Wu, R. T., & Jahanshahi, M. R. (2020). Data fusion approaches for structural health monitoring and system identification: Past, present, and future. *Structural Health Monitoring*, 19(2), 552–586. doi:10.1177/1475921718798769.
- [2] Kot, P., Muradov, M., Gkantou, M., Kamaris, G. S., Hashim, K., & Yeboah, D. (2021). Recent advancements in non-destructive testing techniques for structural health monitoring. *Applied Sciences (Switzerland)*, 11(6), 2750. doi:10.3390/app11062750.
- [3] Caballero-Russi, D., Ortiz, A. R., Guzmán, A., & Canchila, C. (2022). Design and Validation of a Low-Cost Structural Health Monitoring System for Dynamic Characterization of Structures. *Applied Sciences (Switzerland)*, 12(6), 2807. doi:10.3390/app12062807.

- [4] O'Shea, M., & Murphy, J. (2020). Design of a BIM integrated structural health monitoring system for a historic offshore lighthouse. *Buildings*, 10(7), 131. doi:10.3390/BUILDINGS10070131.
- [5] Panah, R. S., & Kioumars, M. (2021). Application of building information modelling (BIM) in the health monitoring and maintenance process: A systematic review. *Sensors (Switzerland)*, 21(3), 1–26. doi:10.3390/s21030837.
- [6] Shults, R. (2022). Geospatial Monitoring of Engineering Structures as a Part of BIM. *International Archives of the Photogrammetry, Remote Sensing and Spatial Information Sciences - ISPRS Archives*, 46(5/W1-2022), 225–230. doi:10.5194/isprs-archives-XLVI-5-W1-2022-225-2022.
- [7] Hamza, V., Stopar, B., Ambrožič, T., Turk, G., & Sterle, O. (2020). Testing multi-frequency low-cost GNSS receivers for geodetic monitoring purposes. *Sensors (Switzerland)*, 20(16), 1–16. doi:10.3390/s20164375.
- [8] Zhao, L., Yang, Y., Xiang, Z., Zhang, S., Li, X., Wang, X., Ma, X., Hu, C., Pan, J., Zhou, Y., & Chen, M. (2022). A Novel Low-Cost GNSS Solution for the Real-Time Deformation Monitoring of Cable Saddle Pushing: A Case Study of Guojiatuo Suspension Bridge. *Remote Sensing*, 14(20), 5174. doi:10.3390/rs14205174.
- [9] Scaioni, M., Marsella, M., Crosetto, M., Tornatore, V., & Wang, J. (2018). Geodetic and remote-sensing sensors for dam deformation monitoring. *Sensors (Switzerland)*, 18(11), 3682. doi:10.3390/s18113682.
- [10] Zschiesche, K. (2021). Image Assisted Total Stations for Structural Health Monitoring—A Review. *Geomatics*, 2(1), 1–16. doi:10.3390/geomatics2010001.
- [11] Doler, D., & Kovačič, B. (2019). Improved decision-making geo-information system for continuous monitoring of deformations on airport infrastructure. *ISPRS International Journal of Geo-Information*, 8(1), 1. doi:10.3390/ijgi8010001.
- [12] Olaszek, P., Maciejewski, E., Rakoczy, A., Cabral, R., Santos, R., & Ribeiro, D. (2024). Remote Inspection of Bridges with the Integration of Scanning Total Station and Unmanned Aerial Vehicle Data. *Remote Sensing*, 16(22), 4176. doi:10.3390/rs16224176.
- [13] Lienhart, W., Ehrhart, M., & Grick, M. (2017). High frequent total station measurements for the monitoring of bridge vibrations. *Journal of Applied Geodesy*, 11(1), 1–8. doi:10.1515/jag-2016-0028.
- [14] Lienhart, W. (2017). Geotechnical monitoring using total stations and laser scanners: critical aspects and solutions. *Journal of Civil Structural Health Monitoring*, 7(3), 315–324. doi:10.1007/s13349-017-0228-5.
- [15] Marenić, A., Paar, R., & Damjanović, D. (2017). Measurement of bridge dynamic displacements and natural frequencies by RTS. *Journal of the Croatian Association of Civil Engineers*, 69(4), 281–294. doi:10.14256/jce.1804.2016.
- [16] Pawlak, Z. M., Wyczałek, I., & Marciniak, P. (2023). Two Complementary Approaches toward Geodetic Monitoring of a Historic Wooden Church to Inspect Its Static and Dynamic Behavior. *Sensors*, 23(20), 8392. doi:10.3390/s23208392.
- [17] Barsocchi, P., Bartoli, G., Betti, M., Girardi, M., Mammolito, S., Pellegrini, D., & Zini, G. (2021). Wireless Sensor Networks for Continuous Structural Health Monitoring of Historic Masonry Towers. *International Journal of Architectural Heritage*, 15(1), 22–44. doi:10.1080/15583058.2020.1719229.
- [18] Corsetti, M., Fossati, F., Manunta, M., & Marsella, M. (2018). Advanced SBAS-DInSAR technique for controlling large civil infrastructures: An application to the Genzano di Lucania dam. *Sensors (Switzerland)*, 18(7), 2371. doi:10.3390/s18072371.
- [19] Wu, S., Zhang, B., Ding, X., Zhang, L., Zhang, Z., & Zhang, Z. (2023). Radar Interferometry for Urban Infrastructure Stability Monitoring: From Techniques to Applications. *Sustainability (Switzerland)*, 15(19), 14654. doi:10.3390/su151914654.
- [20] Teng, J., Lu, W., Cui, Y., & Zhang, R. (2016). Temperature and Displacement Monitoring to Steel Roof Construction of Shenzhen Bay Stadium. *International Journal of Structural Stability and Dynamics*, 16(4), 1640020. doi:10.1142/S0219455416400204.
- [21] Shults, R., Soltabayeva, S., Seitkazina, G., Nukarbekova, Z., & Kucherenko, O. (2020). Geospatial Monitoring and Structural Mechanics Models: a Case Study of Sports Structures. *The 11th International Conference Environmental Engineering 11th ICEE Selected Papers*, enviro.2020.685. doi:10.3846/enviro.2020.685.
- [22] Mukupa, W., Roberts, G. W., Hancock, C. M., & Al-Manasir, K. (2017). A review of the use of terrestrial laser scanning application for change detection and deformation monitoring of structures. *Survey Review*, 49(353), 99–116. doi:10.1080/00396265.2015.1133039.
- [23] Głowacki, T., Grzempowski, P., Sudoł, E., Wajs, J., & Zajac, M. (2017). The assessment of the application of terrestrial laser scanning for measuring the geometrics of cooling towers. *Geomatics, Landmanagement and Landscape*, 4, 49–57. doi:10.15576/gll/2016.4.49.
- [24] Beshr, A. A. A., Basha, A. M., El-Madany, S. A., & El-Azeem, F. A. (2023). Deformation of High Rise Cooling Tower through Projection of Coordinates Resulted from Terrestrial Laser Scanner Observations onto a Vertical Plane. *ISPRS International Journal of Geo-Information*, 12(10), 417. doi:10.3390/ijgi12100417.

- [25] Makuch, M., Gawronek, P., & Mitka, B. (2024). Laser Scanner-Based Hyperboloid Cooling Tower Geometry Inspection: Thickness and Deformation Mapping. *Sensors*, 24(18), 6045. doi:10.3390/s24186045.
- [26] Helming, P., Von Freyberg, A., Sorg, M., & Fischer, A. (2021). Wind turbine tower deformation measurement using terrestrial laser scanning on a 3.4 MW wind turbine. *Energies*, 14(11), 3255. doi:10.3390/en14113255.
- [27] Kregar, K., Ambrožič, T., Kogoj, D., Vežočanik, R., & Marjetič, A. (2015). Determining the inclination of tall chimneys using the TPS and TLS approach. *Measurement*, 75, 354–363. doi:10.1016/j.measurement.2015.08.006.
- [28] Barazzetti, L., Previtali, M., & Roncoroni, F. (2019). The Use of Terrestrial Laser Scanning Techniques to Evaluate Industrial Masonry Chimney Verticality. *The International Archives of the Photogrammetry, Remote Sensing and Spatial Information Sciences*, XLII-2/W11, 173–178. doi:10.5194/isprs-archives-xlii-2-w11-173-2019.
- [29] Siwec, J., & Lenda, G. (2022). Integration of terrestrial laser scanning and structure from motion for the assessment of industrial chimney geometry. *Measurement: Journal of the International Measurement Confederation*, 199, 111404. doi:10.1016/j.measurement.2022.111404.
- [30] Li, Y., Liu, P., Li, H., & Huang, F. (2021). A comparison method for 3D laser point clouds in displacement change detection for arch dams. *ISPRS International Journal of Geo-Information*, 10(3), 184. doi:10.3390/ijgi10030184.
- [31] Ning, X. Y., Zhang, K., Jiang, N., Luo, X. L., Zhang, D. M., Peng, J. W., Luo, X. X., Zheng, Y. S., & Guo, D. (2024). 3D deformation analysis for earth dam monitoring based on terrestrial laser scanning (TLS) and the iterative closest point (ICP) algorithm. *Frontiers in Earth Science*, 12. doi:10.3389/feart.2024.1421705.
- [32] Bolkas, D., O'Banion, M., Laughlin, J., & Prickett, J. (2024). Monitoring of a rockfill embankment dam using TLS and sUAS point clouds. *Journal of Applied Geodesy*, 19(1), 75–93. doi:10.1515/jag-2023-0038.
- [33] Jia, D., Zhang, W., & Liu, Y. (2021). Systematic approach for tunnel deformation monitoring with terrestrial laser scanning. *Remote Sensing*, 13(17), 3519. doi:10.3390/rs13173519.
- [34] Xu, X., Yang, H., & Kargoll, B. (2019). Robust and automatic modeling of tunnel structures based on terrestrial laser scanning measurement. *International Journal of Distributed Sensor Networks*, 15(11), 1-9. doi:10.1177/1550147719884886.
- [35] Cui, L.-Z., Liu, J., Luo, H., Wang, J., Zhang, X., Lv, G., & Xie, Q. (2024). Deformation Measurement of Tunnel Shotcrete Liner Using the Multiepoch LiDAR Point Clouds. *Journal of Construction Engineering and Management*, 150(6), 150. doi:10.1061/jcemd4.coeng-14518.
- [36] Beshr, A. A. A., Ghazi, Z., & Heneash, U. (2025). Condition assessment and inspection of highway bridges using terrestrial laser scanner. *World Journal of Engineering*, 499. doi:10.1108/WJE-09-2024-0499.
- [37] Rashidi, M., Mohammadi, M., Kivi, S. S., Abdolvand, M. M., Truong-Hong, L., & Samali, B. (2020). A decade of modern bridge monitoring using terrestrial laser scanning: Review and future directions. *Remote Sensing*, 12(22), 1–34. doi:10.3390/rs12223796.
- [38] Zhao, Y., Seo, H., & Chen, C. (2021). Displacement mapping of point clouds: application of retaining structures composed of sheet piles. *Journal of Civil Structural Health Monitoring*, 11(4), 915–930. doi:10.1007/s13349-021-00491-y.
- [39] Yang, H., Omidalizarandi, M., Xu, X., & Neumann, I. (2017). Terrestrial laser scanning technology for deformation monitoring and surface modeling of arch structures. *Composite Structures*, 169, 173–179. doi:10.1016/j.compstruct.2016.10.095.
- [40] Nguyen, A. C., & Weinand, Y. (2020). Displacement study of a large-scale freeform timber plate structure using a total station and a terrestrial laser scanner. *Sensors (Switzerland)*, 20(2), 413. doi:10.3390/s20020413.
- [41] Shults, R., Annenkov, A., Seitkazina, G., Soltabayeva, S., Kozhayev, Z., Khailak, A., Nikitenko, K., Sossa, B., & Kulichenko, N. (2022). Analysis of the displacements of pipeline overpasses based on geodetic monitoring results. *Geodesy and Geodynamics*, 13(1), 50–71. doi:10.1016/j.geog.2021.09.005.
- [42] Li, J., Wang, L., & Huang, J. (2023). Wall length-based deformation monitoring method of brick-concrete buildings in mining area using terrestrial laser scanning. *Journal of Civil Structural Health Monitoring*, 13(4–5), 1077–1090. doi:10.1007/s13349-023-00697-2.
- [43] Sun, W., Wang, J., Jin, F., Li, G., & Xu, F. (2023). Intelligent Construction Monitoring Method for Large and Complex Steel Structures Based on Laser Point Cloud. *Buildings*, 13(7), 1749. doi:10.3390/buildings13071749.
- [44] Nap, M. E., Chiorean, S., Cira, C. I., Manso-Callejo, M. Á., Păunescu, V., Şuba, E. E., & Sălăgean, T. (2023). Non-Destructive Measurements for 3D Modeling and Monitoring of Large Buildings Using Terrestrial Laser Scanning and Unmanned Aerial Systems. *Sensors*, 23(12), 5678. doi:10.3390/s23125678.
- [45] Xu, X., Wang, Z., Shi, P., Liu, W., Tang, Q., Bao, X., Chen, X., & Yang, H. (2023). Intelligent monitoring and residual analysis of tunnel point cloud data based on free-form approximation. *Mechanics of Advanced Materials and Structures*, 30(8), 1703–1712. doi:10.1080/15376494.2022.2041775.

- [46] EM 1110-2-1009. (2018). Structural Deformation Surveying. US Army Corps of Engineers, Washington, United States.
- [47] Shults, R. (2021). The Models of Structural Mechanics for Geodetic Accuracy Assignment: A Case Study of the Finite Element Method. Contributions to International Conferences on Engineering Surveying. Springer Proceedings in Earth and Environmental Sciences. Springer, Cham, Switzerland. doi:10.1007/978-3-030-51953-7_16.
- [48] Yang, H., Xu, X., Xu, X., & Liu, W. (2024). TLS and FEM combined methods for deformation analysis of tunnel structures. Mechanics of Advanced Materials and Structures, 31(6), 1264–1271. doi:10.1080/15376494.2022.2134613.
- [49] Korumaz, M., Betti, M., Conti, A., Tucci, G., Bartoli, G., Bonora, V., Korumaz, A. G., & Fiorini, L. (2017). An integrated Terrestrial Laser Scanner (TLS), Deviation Analysis (DA) and Finite Element (FE) approach for health assessment of historical structures. A minaret case study. Engineering Structures, 153, 224–238. doi:10.1016/j.engstruct.2017.10.026.
- [50] Takhirov, S., Rakhmonov, B., Nafasov, R., Samandarov, A., & Sultanova, S. (2023). Laser Scanning and Ambient Vibration Study of Juma Mosque in Khiva (Uzbekistan) with Subsequent Finite Element Modeling of Its Minaret. Remote Sensing, 15(6), 1632. doi:10.3390/rs15061632.
- [51] Kermarrec, G., Kargoll, B., & Alkhatib, H. (2020). Deformation analysis using B-spline surface with correlated terrestrial laser scanner observations—a bridge under load. Remote Sensing, 12(5), 829. doi:10.3390/rs12050829.
- [52] Xu, H., Li, H., Yang, X., Qi, S., & Zhou, J. (2019). Integration of terrestrial laser scanning and NURBS modeling for the deformation monitoring of an earth-rock dam. Sensors (Switzerland), 19(1), 22. doi:10.3390/s19010022.
- [53] Harmening, C. (2020). Spatio-temporal deformation analysis using enhanced B-spline models of laser scanning point clouds. PhD Thesis, Technische Universität Wien, Vienna, Austria.
- [54] Harmening, C., Hobmaier, C., & Neuner, H. (2021). Laser scanner-based deformation analysis using approximating b-spline surfaces. Remote Sensing, 13(18), 3551. doi:10.3390/rs13183551.
- [55] Bureick, J., Alkhatib, H., & Neumann, I. (2016). Robust Spatial Approximation of Laser Scanner Point Clouds by Means of Free-form Curve Approaches in Deformation Analysis. Journal of Applied Geodesy, 10(1), 27–35. doi:10.1515/jag-2015-0020.
- [56] Xu, X., Kargoll, B., Bureick, J., Yang, H., Alkhatib, H., & Neumann, I. (2018). TLS-based profile model analysis of major composite structures with robust B-spline method. Composite Structures, 184, 814–820. doi:10.1016/j.compstruct.2017.10.057.
- [57] Xu, J., Ding, L., Luo, H., Chen, E. J., & Wei, L. (2019). Near real-time circular tunnel shield segment assembly quality inspection using point cloud data: A case study. Tunnelling and Underground Space Technology, 91. doi:10.1016/j.tust.2019.102998.
- [58] Kermarrec, G., Schild, N., & Hartmann, J. (2021). Fitting terrestrial laser scanner point clouds with t-splines: Local refinement strategy for rigid body motion. Remote Sensing, 13(13), 2494. doi:10.3390/rs13132494.
- [59] Shults, R., Seitkazina, G., & Soltabayeva, S. (2023). The Features of Sports Complex “Sunkar” Monitoring By Terrestrial Laser Scanning. International Archives of the Photogrammetry, Remote Sensing and Spatial Information Sciences - ISPRS Archives, 48(5/W2-2023), 105–110. doi:10.5194/isprs-archives-XLVIII-5-W2-2023-105-2023.
- [60] Logan, D.L. (2011) A First Course in the Finite Element Method. 5th Edition, Thomson, Toronto, Canada.
- [61] Lee, H. H. (2012). Finite element simulations with ANSYS Workbench 14. SDC publications, Mission, Canada.
- [62] Liu, G.R. and Quek, S.S. (2003) The Finite Element Method: A Practical Course. Butterworth-Heinemann, New York, United States.
- [63] Connor, J. J., & Faraji, S. (2013). Fundamentals of Structural Engineering. Springer New York, United States. doi:10.1007/978-1-4614-3262-3.
- [64] Cadence Design Systems (2025). An Introduction to B-Spline Curves. Cadence Design Systems, California, United States. Available online: <https://resources.system-analysis.cadence.com/blog/msa2022-an-introduction-to-b-spline-curves> (accessed on February 2025).
- [65] Perperoglou, A., Sauerbrei, W., Abrahamowicz, M., & Schmid, M. (2019). A review of spline function procedures in R. BMC Medical Research Methodology, 19(1), 46. doi:10.1186/s12874-019-0666-3.
- [66] MTU (2025). NURBS: Definition. Michigan Technological University, Michigan, United States. Available online: <https://pages.mtu.edu/~shene/COURSES/cs3621/NOTES/spline/NURBS/NURBS-def.html> (accessed on February 2025).
- [67] Piegl, L., & Tiller, W. (1995). The NURBS Book: Monographs in Visual Communication (VISUALCOMM). Springer-Verlag, Berlin/Heidelberg, Germany. doi:10.1007/978-3-642-97385-7.